

Quantum Gauge Networks: A New Kind of Tensor Network

Kevin Slagle^{1,2,3}

¹*Department of Electrical and Computer Engineering,
Rice University, Houston, Texas 77005 USA*

²*Department of Physics, California Institute of Technology,
Pasadena, California 91125, USA*

³*Institute for Quantum Information and Matter and Walter Burke Institute for Theoretical Physics,
California Institute of Technology,
Pasadena, California 91125, USA*

Although tensor networks are powerful tools for simulating low-dimensional quantum physics, tensor network algorithms are very computationally costly in higher spatial dimensions. We introduce *quantum gauge networks*: a different kind of tensor network ansatz for which the computation cost of simulations does not explicitly increase for larger spatial dimensions. We take inspiration from the gauge picture of quantum dynamics [1], which consists of a local wavefunction for each patch of space, with neighboring patches related by unitary connections. A quantum gauge network (QGN) has a similar structure, except the Hilbert space dimensions of the local wavefunctions and connections are truncated. We describe how a QGN can be obtained from a generic wavefunction or matrix product state (MPS). All $2k$ -point correlation functions of any wavefunction for M many operators can be encoded exactly by a QGN with bond dimension $O(M^k)$. In comparison, for just $k = 1$, an exponentially larger bond dimension of $2^{M/6}$ is generically required for an MPS of qubits. We provide a simple QGN algorithm for approximate simulations of quantum dynamics in any spatial dimension. The approximate dynamics can achieve exact energy conservation for time-independent Hamiltonians, and spatial symmetries can also be maintained exactly. We benchmark the algorithm by simulating the quantum quench of fermionic Hamiltonians in up to three spatial dimensions.

Tensor network algorithms [2–7] are very useful for simulating strongly-correlated quantum physics. In one spatial dimension, matrix product state (MPS) algorithms [3–5] are often the best available tool for this task. Although still useful, tensor network algorithms in higher dimensions [3, 5, 8–15] typically suffer from computational costs that scale as a high power of the bond dimension. Therefore, we are motivated to study a different kind of tensor network ansatz that is more computationally efficient in many spatial dimensions.

We take inspiration from the gauge picture of quantum dynamics [1]. In the gauge picture, one first chooses a collection of possibly-overlapping patches of space that cover space. For example, one could choose the patches to be pairs of nearest-neighbor sites on a lattice. We use capital letters, I , J , or K , to denote a spatial patch. The Hamiltonian is written as a sum over terms \hat{H}_I that act within a single patch I :

$$\hat{H} = \sum_I \hat{H}_I \quad (1)$$

Each patch is assigned a *local wavefunction* $|\Psi_I\rangle$, and the Hilbert spaces of neighboring patches are related by unitary connections \hat{U}_{IJ} . The local wavefunctions and connections time-evolve according to

$$\begin{aligned} \partial_t |\Psi_I\rangle &= -i\hat{H}_{\langle I} |\Psi_I\rangle \\ \partial_t \hat{U}_{IJ} &= -i\hat{H}_{\langle I} \hat{U}_{IJ} + i\hat{U}_{IJ} \hat{H}_{\langle J} \end{aligned} \quad (2)$$

where

$$\hat{H}_{\langle I} = \sum_J^{J \cap I \neq \emptyset} \hat{U}_{IJ} \hat{H}_J \hat{U}_{JI} \quad (3)$$

is the sum of local Hamiltonian terms supported on patches that overlap with patch I . The main feature of the gauge picture is that spatial locality is explicit in the above equations of motion. Typically, we initialize $\hat{U}_{IJ}(0) = \hat{1}$ and $|\Psi_I(0)\rangle = |\Psi(0)\rangle$ at time $t = 0$, where $\hat{1}$ is the identity operator and $|\Psi(t)\rangle$ is the usual wavefunction in the Schrödinger picture. The expectation value $\langle \Psi | \hat{A}_I | \Psi \rangle$ of a local operator \hat{A}_I that only acts within the patch I can be evaluated in the gauge picture as $\langle \Psi_I | \hat{A}_I | \Psi_I \rangle$. To calculate an expectation value $\langle \Psi | \hat{A}_I \hat{B}_J | \Psi \rangle$ for a product of operators acting on different patches, a connection \hat{U}_{IJ} must be inserted in the gauge picture, as in $\langle \Psi_I | \hat{A}_I \hat{U}_{IJ} \hat{B}_J | \Psi_J \rangle$. Time evolution preserves the following network of relations:

$$\begin{aligned} \hat{U}_{IJ} |\Psi_J\rangle &= |\Psi_I\rangle \\ \hat{U}_{IJ} \hat{U}_{JK} &= \hat{U}_{IK} \end{aligned} \quad (4)$$

along with $\hat{U}_{IJ}^\dagger = \hat{U}_{JI}$ and $\hat{U}_{II} = \hat{1}$.

In this work, we truncate the Hilbert spaces of the local wavefunctions and connections so that approximate quantum simulations can be performed on a computer. The utility of the gauge picture for approximating quantum mechanics is that locality is explicit in

both the time dynamics and the structure of the local wavefunctions and connections. We call the resulting network of truncated local wavefunctions and connections a *quantum gauge network* (QGN).

An advantage of quantum gauge networks is that unlike traditional tensor networks (e.g. PEPS [3]), a QGN only involves matrices and vectors regardless of the spatial dimension. As such, many QGN calculations only require a computation time (e.g. CPU time) that scales as $O(\chi^3)$, regardless of the number of spatial dimensions, where χ is the dimension of the truncated Hilbert spaces. χ can be viewed as the bond dimension of the QGN. The $O(\chi^3)$ computation time for a QGN is the same as MPS algorithms, which are very efficient in one spatial dimension (1D). In three spatial dimensions (3D), the most computationally efficient tensor network in previous literature may be the isometric tensor network [8–10], for which the computation time of the TEBD³ algorithm is $O(\chi^{12})$ [11].¹ Thus, quantum gauge network algorithms can require significantly less computation time for fixed bond dimension. This is useful since larger bond dimensions allow more correlations to be transported through the tensor network. The computation time per variational parameter also scales favorably for QGN algorithms.²

Although most tensor networks typically directly encode a wavefunction or density matrix, a QGN departs from this habit. Indeed, in the gauge picture, only local correlation functions $\langle \Psi_I | \hat{A}_I | \Psi_I \rangle$ can be extracted from the local wavefunctions if we do not make use of the connections \hat{U}_{IJ} . Long range entanglement is then encoded within the connections. Unlike a generic PEPS [3] but similar to a matrix product state (MPS) or isometric tensor network [8–10], local expectation values can be efficiently computed from a QGN. A disadvantage of quantum gauge networks is that unphysical states can also be encoded. As such, using a QGN to variationally optimize a ground state is not as straight-forward as for tensor networks that directly encode a wavefunction. We leave QGN ground state optimization algorithms to future work. In this work, we focus on QGN fundamentals and time dynamics algorithms.

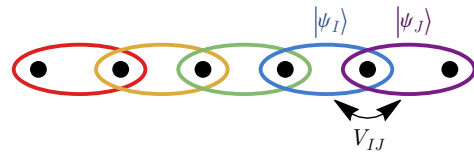


FIG. 1. An example of a chain of qubits (black dots) and spatial patches (colored ovals) consisting of pairs of neighboring qubits. A local wavefunction $|\psi_I\rangle$ is associated with each patch I , and the Hilbert spaces of neighboring patches are related by connections V_{IJ} .

In Sec. I, we discuss basic properties of quantum gauge networks and how a QGN can be constructed. We also show that for an arbitrary wavefunction (including fermionic wavefunctions), all $2k$ -point correlation functions of M many operators can be encoded exactly by a QGN with bond dimension $O(M^k)$ [Eq. (31)], while an MPS of qubits can require an exponentially larger bond dimension $2^{M/6}$ for $k = 1$. In Sec. II, we present a QGN algorithm for approximately simulating quantum dynamics in the gauge picture. We benchmark the algorithm using simulations of fermionic Hamiltonians in spatial dimensions up to three.

I. QUANTUM GAUGE NETWORKS

To define a quantum gauge network (QGN), we first choose a collection of possibly-overlapping patches of space that cover space. For example, one could choose the patches to be nearest-neighbor sites on a lattice, or each patch could consist of just a single lattice site. A QGN then consists of (1) a *local wavefunction* $|\psi_I\rangle$ for each spatial patch; (2) non-unitary *connections* $V_{IJ} = V_{JI}^\dagger$ to relate the Hilbert spaces of nearby patches, as depicted in Fig. 1; and (3) a collection of truncated operators to act on the truncated Hilbert space at each patch.

The local wavefunctions and connections are similar to the those within the gauge picture [1], except the Hilbert space is truncated. If the full Hilbert space has dimension N , then $|\Psi_I\rangle$ and \hat{U}_{IJ} in the gauge picture have dimensions N and $N \times N$, respectively. Since N is exponentially large in system size, it is useful to truncate the full Hilbert space dimension for approximate simulations. Therefore, we consider truncated local wavefunctions $|\psi_I\rangle$ and connections V_{IJ} , which have truncated dimensions χ_I and $\chi_I \times \chi_J$, respectively, where typically $\chi_I \ll N$. We use capital and lower-case Greek letters (e.g. $|\Psi_I\rangle$ vs $|\psi_I\rangle$) for wavefunctions in the full and truncated Hilbert spaces, respectively. Similarly, we place hats on operators that act within the full Hilbert space (e.g. \hat{U}_{IJ}), while operators within the truncated Hilbert space (e.g. V_{IJ}) do not have hats.

In order to calculate expectation values of local

¹ More generally, the TEBD³ computation time is $O(D^{10}\chi^2) + O(D\chi^6)$ when the bond dimension χ of the central bonds is different from the bond dimension D of the other bonds. [11] In 2D, the TEBD² computation time scales as χ^7 . [8]

² The number of variational parameters can differ significantly for different tensor networks. Therefore, it is also useful to compare the scaling of the computation time per variational parameter. For a QGN, the number of parameters scales as χ^2 (due to the matrix-valued connections). Therefore, the computation time per parameter scales as $\chi^3/\chi^2 = \chi^{1.5}$ for a QGN. This is the same ratio as MPS algorithms, which are very efficient in 1D. For the isometric tensor network TEBD³ algorithm in 3D, this ratio scales as $\chi^{12}/\chi^6 = \chi^2$ [11], which is remarkably efficient but not as good as the ratio for a QGN or MPS.

operators \hat{A}_I in the original Hilbert space, we must also define truncated operators, i.e. $\chi_I \times \chi_I$ matrices A_I , that act on the truncated Hilbert space. Throughout this work, \hat{A}_I always denotes an operator that acts within a patch I , and similar for \hat{B}_J , etc. The truncated operators A_I are notationally distinguished from the original operators \hat{A}_I by the lack of a hat. In Sec. IA, we present a concrete mapping to obtain a QGN and truncated operators. However, in many cases (e.g. Appendix C1a and E) the truncated operators can be taken to be a simple Kronecker product, such as $\sigma_I^\mu = \mathbb{1} \otimes \sigma^\mu$, where $\mathbb{1}$ is an identity matrix and σ^μ is a 2×2 Pauli matrix.

Ideally, we want the quantum gauge network to accurately encode approximate expectation values. For example, if the QGN is an approximation for a wavefunction $|\Psi\rangle$, then we would like the QGN to accurately encode local expectation values; i.e. we want $\langle \psi_I | A_I | \psi_I \rangle \approx \langle \Psi | \hat{A}_I | \Psi \rangle$. Similarly, we typically also want expectation values of string operators to also approximately match, e.g.

$$\langle \psi_I | A_I V_{IJ} B_J V_{JK} C_K | \psi_K \rangle \approx \langle \Psi | \hat{A}_I \hat{B}_J \hat{C}_K | \Psi \rangle \quad (5)$$

Note that in order to express a string operator that acts on multiple spatial patches using a QGN, it is essential to insert connections V_{IJ} between operators and wavefunctions associated with different spatial patches.

Similar to the gauge picture of quantum dynamics, quantum gauge networks also exhibit a local gauge symmetry:

$$\begin{aligned} |\psi_I\rangle &\rightarrow \Lambda_I |\Psi_I\rangle \\ V_{IJ} &\rightarrow \Lambda_I V_{IJ} \Lambda_J^\dagger \\ A_I &\rightarrow \Lambda_I A_I \Lambda_I^\dagger \end{aligned} \quad (6)$$

where Λ_I is a unitary matrix. Expectation values must be invariant under this symmetry.

Since local expectation values $\langle \Psi | \hat{A}_I | \Psi \rangle \approx \langle \psi_I | A_I | \psi_I \rangle$ are encoded in the local wavefunctions $|\psi_I\rangle$, we can think of the local wavefunction as a purified reduced density matrix for a spatial patch. The connections V_{IJ} encode long-range correlations between the spatial patches.

It is desirable for a QGN to at least approximately obey the following consistency conditions

$$\begin{aligned} V_{IJ} |\psi_J\rangle &\approx |\psi_I\rangle \\ V_{IJ} V_{JK} &\approx V_{IK} \end{aligned} \quad (7)$$

Although it is easy to make the first relation exact, the second will typically only hold approximately. Typically, a QGN will only possess a V_{IJ} for nearby patches I and J (and not for far away patches). Thus, the second relation only applies if all three connections (V_{IJ} , V_{JK} , and V_{IK}) are contained in the QGN. The connections V_{IJ} should have singular values between 0 and 1 (to ensure

that expectation values are never larger than the largest eigenvalue of the measured operator).

When $V_{IJ} |\psi_J\rangle = |\psi_I\rangle$ holds exactly, QGN connected correlation functions obey the usual identity (with a V_{IJ} inserted):

$$\begin{aligned} &\langle \psi_I | (A_I - \langle A_I \rangle) V_{IJ} (B_J - \langle B_J \rangle) | \psi_J \rangle \\ &= \langle \psi_I | A_I V_{IJ} B_J | \psi_J \rangle - \langle A_I \rangle \langle B_J \rangle \end{aligned} \quad (8)$$

where we abbreviate $\langle A_I \rangle = \langle \psi_I | A_I | \psi_I \rangle$ and $\langle B_J \rangle = \langle \psi_J | B_J | \psi_J \rangle$. Therefore, if the QGN connected correlation function [Eq. (8)] is small, we are guaranteed that $\langle \psi_I | A_I V_{IJ} B_J | \psi_J \rangle \approx \langle A_I \rangle \langle B_J \rangle$, as one should expect. The equations in this paragraph also hold for longer chains of connections; e.g. they also hold if we replace V_{IJ} with $V_{IK} V_{KL} V_{LI}$.

A. QGN from Truncation Maps

In this subsection, we study a concrete construction to obtain a quantum gauge network. The input for this QGN construction is a wavefunction $|\Psi\rangle$, along with a *truncation map* Q_I for each patch of space. If we want to construct a QGN from a density matrix instead, then $|\Psi\rangle$ should be chosen to be a purification of the density matrix. The truncation maps are $\chi_I \times N$ matrices that satisfy:

$$\begin{aligned} Q_I Q_I^\dagger &= \hat{\mathbb{1}} \\ Q_I^\dagger Q_I |\Psi\rangle &= |\Psi\rangle \end{aligned} \quad (9)$$

Therefore Q_I^\dagger is an isometry matrix whose image includes the wavefunction. (A matrix M is isometric if $M^\dagger M = \mathbb{1}$.) Intuitively, each Q_I maps a select subspace of states into a truncated Hilbert space. In the next subsection, we will explain how one can obtain useful truncation maps.

With this data, we can construct the following QGN:

$$\begin{aligned} |\psi_I\rangle &= Q_I |\Psi\rangle \\ V_{IJ} &= Q_I Q_J^\dagger \end{aligned} \quad (10)$$

Note that $V_{II} = \mathbb{1}$ due to Eq. (9). Local operators \hat{A}_I with support on a spatial patch I are also truncated:

$$A_I = Q_I \hat{A}_I Q_I^\dagger \quad (11)$$

Note that this equation can be used for both bosonic and fermionic operators.

The resulting connections V_{IJ} have singular values between 0 and 1. One can verify that

$$V_{IJ} |\psi_J\rangle = |\psi_I\rangle \quad (12)$$

from Eq. (7) holds exactly.

In practice, the truncation mapping can only be directly applied for wavefunctions that are simple enough such that the truncation can be efficiently computed. However, the construction is also useful for theoretically understanding how a QGN can encode a wavefunction.

A trivial example of a QGN can be obtained from a product state wavefunction $|\Psi\rangle = |\psi_1\rangle \otimes |\psi_2\rangle \otimes \dots \otimes |\psi_n\rangle$. The truncation maps can be chosen to be $Q_I = |\psi_I\rangle \langle \Psi|$, with $I = 1, \dots, n$. This results in a QGN with local wavefunctions $|\psi_I\rangle$ and connections $V_{IJ} = |\psi_I\rangle \otimes \langle \psi_J|$. The truncated operators simply act within the on-site Hilbert space. Additional examples of quantum gauge networks can be found in Appendix C.

Note that not all quantum gauge networks can be obtained from the truncation mapping. For example, generating a QGN by sampling random numbers for $|\psi_I\rangle$ and V_{IJ} will result in a very unphysical QGN that is not consistent with any wavefunction. This is in contrast to MPS or PEPS tensor networks, for which a random number initialization still returns a physical (although unnormalized) wavefunction.

In Appendix B, we show how to obtain truncation maps from the canonical form of a matrix product state (MPS) [3–5]. If the MPS has bond dimension χ , then the QGN will have bond dimensions equal to $d\chi^2$, where d is the Hilbert space dimension at each site. ($d = 2$ for qubits.) The idea of the mapping is that the canonical form of an MPS can consist of a center tensor at I that is surrounded by isometric tensors. The isometric tensors are then used to construct a truncation map Q_I , while the center tensor is a local wavefunction $|\psi_I\rangle$.

In the limit that the bond dimension $\chi_I \rightarrow N$ approaches the full Hilbert space dimension N , the truncation mapping [Eqs. (10) and (11)] will result in a QGN that encodes correlation functions [e.g. Eq. (5)] exactly. A nice guarantee made by the truncation mapping is that the norm of expectation values is never overestimated; e.g.

$$\left| \langle \psi_I | A_I V_{IJ} B_J V_{JK} C_K | \psi_K \rangle \right| \leq \left| \langle \Psi | \hat{A}_I \hat{B}_J \hat{C}_K | \Psi \rangle \right| \quad (13)$$

This follows from Eq. (10) and the fact that Q_I^\dagger is isometric, which implies that $|\langle \Theta | Q_I^\dagger Q_I | \Phi \rangle| \leq |\langle \Theta | \Phi \rangle|$ for all wavefunctions $|\Theta\rangle$ and $|\Phi\rangle$. Note that Eq. (13) also applies to connected correlation functions, such as the first line of Eq. (8).

B. Truncation Map Construction

The accuracy of the truncation critically depends on a good choice of truncation maps Q_I . Suppose we want to choose truncation maps such that the quantum gauge network exactly encodes the expectation values of a chosen collection of operator strings. For example, the

expectation value of $\hat{A}_I \hat{B}_J \hat{C}_K$ is encoded exactly if

$$\langle \psi_I | A_I V_{IJ} B_J V_{JK} C_K | \psi_K \rangle = \langle \Psi | \hat{A}_I \hat{B}_J \hat{C}_K | \Psi \rangle \quad (14)$$

Below, we show that this exact encoding can be achieved by choosing truncation maps such that the image of each Q_I^\dagger is the span of certain strings of operators involved in the expectation values.

In general, we will find that the required bond dimension χ_I for each patch I is bounded by $\chi_I \leq 1 + 2p_I$ [Eq. (22)], where p_I is the number of chosen operator strings (which we want to encode) that act on the patch I . Note that if we are satisfied with encoding expectation values within some error ϵ , then we can omit operator strings with expectation values less than ϵ from the collection since the truncation never increases the absolute value of expectation values [Eq. (13)]. We also find that bond dimension $O(M^k)$ [Eq. (31)] is sufficient to exactly encode all $2k$ -point correlation functions of M different operators.

1. Warmup Example

Before presenting a generic algorithm for obtaining the truncation maps, let us first discuss an instructive example. Suppose we want to ensure that the QGN encodes the expectation value in Eq. (14) exactly for a particular choice of local operators (\hat{A}_I , \hat{B}_J , and \hat{C}_K) and spatial patches $I \neq J \neq K$. Below, we show that any choice of truncation maps with the following images is sufficient:

$$\begin{aligned} \text{im}(Q_I^\dagger) &= \text{span}\{|\Psi\rangle, \hat{A}_I^\dagger |\Psi\rangle\} \\ \text{im}(Q_J^\dagger) &= \text{span}\{|\Psi\rangle, \hat{A}_I^\dagger |\Psi\rangle, \hat{C}_K |\Psi\rangle\} \\ \text{im}(Q_K^\dagger) &= \text{span}\{|\Psi\rangle, \hat{C}_K |\Psi\rangle\} \end{aligned} \quad (15)$$

$\text{span}\{|\Psi_1\rangle, \dots, |\Psi_m\rangle\}$ denotes the vector space spanned by the vectors $|\Psi_1\rangle, \dots, |\Psi_m\rangle$. We set the bond dimensions to be equal to the vector space dimension of the images: $\chi_I = \dim(\text{im}(Q_I^\dagger))$. Specifying these images determines the truncation maps Q_I up to a unitary gauge transformation $Q_I \rightarrow \Lambda_I Q_I$, where Λ_I is a unitary matrix. The choice of gauge does not affect QGN expectation values. For examples of a quantum gauge networks obtained in this way, see Appendix C.

On a computer, a Q_I^\dagger with the desired image can be calculated from the compact singular value decomposition $M_I = Q_I^\dagger S_I R_I$. Here, M_I is a matrix of column vector, which each encode one of the wavefunctions contained in the span of $\text{im}(Q_I^\dagger)$. S_I is a $\chi_I \times \chi_I$ diagonal matrix of nonzero singular values, and R_I^\dagger is an isometry matrix.

Note that if $|\Phi\rangle \in \text{im}(Q_I^\dagger)$, then $Q_I^\dagger Q_I |\Phi\rangle = |\Phi\rangle$, which is a useful property. This follows because $|\Phi\rangle \in \text{im}(Q_I^\dagger)$ implies that there exists $|\phi\rangle$ such

that $Q_I^\dagger|\phi\rangle = |\Phi\rangle$, which then implies that $Q_I^\dagger Q_I|\Phi\rangle = Q_I^\dagger Q_I Q_I^\dagger|\phi\rangle = Q_I^\dagger|\phi\rangle = |\Phi\rangle$ where the middle equality follows from $Q_I Q_I^\dagger = \hat{1}$ [Eq. (9)].

For each patch, the image must contain $|\Psi\rangle$ so that Eq. (9) is satisfied. Next, we show that Eq. (15) is sufficient to exactly encode the expectation value in Eq. (14):

$$\begin{aligned}
& \langle \psi_I | A_I V_{IJ} B_J V_{JK} C_K | \psi_K \rangle \\
&= \langle \Psi | Q_I^\dagger (Q_I \hat{A}_I Q_I^\dagger) V_{IJ} B_J V_{JK} (Q_K \hat{C}_K Q_K^\dagger) Q_K | \Psi \rangle \\
&= \langle \Psi | \hat{A}_I Q_I^\dagger V_{IJ} B_J V_{JK} Q_K \hat{C}_K | \Psi \rangle \\
&= \langle \Psi | \hat{A}_I Q_I^\dagger (Q_I Q_J^\dagger) B_J (Q_J Q_K^\dagger) Q_K \hat{C}_K | \Psi \rangle \\
&= \langle \Psi | \hat{A}_I Q_J^\dagger B_J Q_J \hat{C}_K | \Psi \rangle \\
&= \langle \Psi | \hat{A}_I Q_J^\dagger (Q_J \hat{B}_J Q_J^\dagger) Q_J \hat{C}_K | \Psi \rangle \\
&= \langle \Psi | \hat{A}_I \hat{B}_J \hat{C}_K | \Psi \rangle
\end{aligned} \tag{16}$$

We used the identities $|\psi_I\rangle = Q_I|\Psi\rangle$ and $V_{IJ} = Q_I Q_J^\dagger$ [Eq. (10)], $A_I = Q_I \hat{A}_I Q_I^\dagger$ [Eq. (11)], and $Q_I^\dagger Q_I|\Phi\rangle = |\Phi\rangle$ whenever $|\Phi\rangle \in \text{im}(Q_I^\dagger)$ in Eq. (15).

Note that even if all the local operators commute, the path of the string matters. For example, Eq. (15) does not guarantee that $\langle \psi_I | B_J V_{JI} A_I V_{IK} C_K | \psi_K \rangle = \langle \Psi | \hat{B}_J \hat{A}_I \hat{C}_K | \Psi \rangle$ even if $[\hat{A}_I, \hat{B}_J] = 0$.

If we want the QGN to encode expectation values for multiple operator strings, then we must calculate the images for each operator string, and then take the union. For example, if two operator strings respectively require $\text{im}(Q_I^\dagger) \supseteq S_I^{(1)}$ and $\text{im}(Q_I^\dagger) \supseteq S_I^{(2)}$, then we need $\text{im}(Q_I^\dagger) \supseteq \text{span}(S_I^{(1)}, S_I^{(2)})$.

Equation (15) is not the unique choice for the images. For instance, the images could be larger. That is, it is sufficient to replace the equalities “=” in Eq. (15) with superset relations “ \supseteq ”. Alternatively, we could replace $\text{im}(Q_I^\dagger)$ with

$$\text{im}(Q_I^\dagger) = \text{span}\{|\Psi\rangle, \hat{B}_J \hat{C}_K |\Psi\rangle, \hat{C}_K |\Psi\rangle\} \tag{17}$$

And with this $\text{im}(Q_I^\dagger)$, we could then replace $\text{im}(Q_I^\dagger)$ with

$$\text{im}(Q_I^\dagger) = \text{span}\{|\Psi\rangle, \hat{B}_J \hat{C}_K |\Psi\rangle\} \tag{18}$$

The proof is similar to Eq. (16). By comparing these choices, we see that we have some freedom in choosing a midpoint in the string of operator products, which we make explicit in the generic case below.

2. Generic Case

More generally, suppose we want to ensure that a QGN exactly encodes the expectation value of $\hat{A}_{I_1}^{(1)} \hat{A}_{I_2}^{(2)} \dots \hat{A}_{I_M}^{(M)}$, which is a product of M local

operators. This expectation value is exactly encoded in the QGN if

$$\begin{aligned}
& \langle \psi_{I_1} | A_{I_1}^{(1)} V_{I_1, I_2} A_{I_2}^{(2)} V_{I_2, I_3} \dots A_{I_M}^{(M)} | \psi_{I_M} \rangle \\
&= \langle \Psi | \hat{A}_{I_1}^{(1)} \hat{A}_{I_2}^{(2)} \dots \hat{A}_{I_M}^{(M)} | \Psi \rangle
\end{aligned} \tag{19}$$

where I_1, \dots, I_m is a string of neighboring patches with $I_m \neq I_{m+1}$. The exact encoding [Eq. (19)] is guaranteed by any choice of truncation maps with images that contain:

$$\text{im}(Q_{I_m}^\dagger) \supseteq \begin{cases} \text{span}\{|\Psi\rangle, |\Psi_{m-1}^L\rangle, |\Psi_m^L\rangle\} & m < m_0 \\ \text{span}\{|\Psi\rangle, |\Psi_{m-1}^L\rangle, |\Psi_{m+1}^R\rangle\} & m = m_0 \\ \text{span}\{|\Psi\rangle, |\Psi_m^R\rangle, |\Psi_{m+1}^R\rangle\} & m > m_0 \end{cases} \tag{20}$$

where we recursively define

$$\begin{aligned}
|\Psi_0^L\rangle &= |\Psi_{M+1}^R\rangle = |\Psi\rangle \\
|\Psi_m^L\rangle &= \hat{A}_{I_m}^{(m)\dagger} |\Psi_{m-1}^L\rangle \\
|\Psi_m^R\rangle &= \hat{A}_{I_m}^{(m)} |\Psi_{m+1}^R\rangle
\end{aligned} \tag{21}$$

In Eq. (20), we are free to choose any half-integer $m_0 = 1, \frac{3}{2}, \dots, M$ between 1 and M .

As noted previously, if we want the QGN to encode expectation values for M different operator strings, then for each image we obtain a list of conditions $\text{im}(Q_I^\dagger) \supseteq S_I^{(m)}$ from Eq. (20) with $m = 1, 2, \dots, M$. We can then take the images to be the span of these vector spaces: $\text{im}(Q_I^\dagger) = \text{span}(S_I^{(1)}, S_I^{(2)}, \dots, S_I^{(M)})$.

We can easily bound the necessary bond dimensions χ_I needed to exactly encode the expectation values for many operator strings. Let p_I be the number of operator strings that involve the spatial patch I . Each application of Eq. (20) increases the dimension of $\text{im}(Q_I^\dagger)$ by at most 2 [starting from $\chi_I = 1$ since we always have $|\Psi\rangle \in \text{im}(Q_{I_m}^\dagger)$]. Therefore, this procedure results in bond dimensions of at most

$$\chi_I \leq 1 + 2p_I \tag{22}$$

To prove that Eq. (20) implies Eq. (19), we first recall that $Q_I^\dagger Q_I|\Phi\rangle = |\Phi\rangle$ whenever $|\Phi\rangle \in \text{im}(Q_I^\dagger)$. We thus obtain

$$\begin{aligned}
& \langle \psi_{I_1} | A_{I_1}^{(1)} V_{I_1, I_2} \dots A_{I_{\lceil m_0 \rceil - 1}}^{(\lceil m_0 \rceil - 1)} Q_{\lceil m_0 \rceil - 1} \\
&= \langle \Psi_{I_1} | \hat{A}_{I_1}^{(1)} \dots \hat{A}_{I_{\lceil m_0 \rceil - 1}}^{(\lceil m_0 \rceil - 1)}
\end{aligned} \tag{23}$$

and

$$\begin{aligned}
& Q_{\lceil m_0 \rceil + 1}^\dagger A_{\lceil m_0 \rceil + 1}^{(\lceil m_0 \rceil + 1)} \dots V_{I_{M-1}, I_M} A_{I_M}^{(M)} | \psi_{I_M} \rangle \\
&= \hat{A}_{\lceil m_0 \rceil + 1}^{(\lceil m_0 \rceil + 1)} \dots \hat{A}_{I_M}^{(M)} | \Psi \rangle
\end{aligned} \tag{24}$$

by again using the identities $|\psi_I\rangle = Q_I|\Psi\rangle$, $V_{IJ} = Q_I Q_J^\dagger$, and $A_I = Q_I \hat{A}_I Q_I^\dagger$. If m_0 is an integer, then inserting

$V_{m_0-1, m_0} A_{m_0} V_{m_0, m_0+1} = Q_{m_0-1} Q_{m_0}^\dagger A_{m_0} Q_{m_0} Q_{m_0+1}^\dagger$
and Eqs. (23) and (24) into the first line of Eq. (19) yields

$$\begin{aligned} & \langle \psi_{I_1} | A_{I_1}^{(1)} V_{I_1, I_2} \cdots A_{I_M}^{(M)} | \psi_{I_M} \rangle \\ &= \langle \Psi | \hat{A}_{I_1}^{(1)} \cdots \hat{A}_{I_{m_0-1}}^{(m_0-1)} (Q_{m_0}^\dagger Q_{m_0} \hat{A}_{m_0} Q_{m_0}^\dagger Q_{m_0}) \\ & \quad \hat{A}_{I_{m_0+1}}^{(m_0+1)} \cdots \hat{A}_{I_M}^{(M)} | \Psi \rangle \\ &= \langle \Psi | \hat{A}_{I_1}^{(1)} \cdots \hat{A}_{I_M}^{(M)} | \Psi \rangle \end{aligned} \quad (25)$$

If m_0 is a half-integer, then Eq. (19) follows immediately from $V_{\lfloor m_0 \rfloor, \lceil m_0 \rceil} = Q_{\lfloor m_0 \rfloor}^\dagger Q_{\lceil m_0 \rceil}$ and Eqs. (23) and (24). This completes the proof.

3. Long-Range Correlation Functions

We can now show that quantum gauge networks can efficiently encode long-range correlation functions. Suppose we want a QGN to exactly encode all two-point correlation functions for some arbitrary collection of operators $\hat{\tau}_i^\mu$ (indexed by μ and position i). That is, suppose we want a QGN to satisfy

$$\langle \psi_I | \tau_{i \in I}^{\mu \dagger} V_{IJ}^{\text{string}} \tau_{j \in J}^\nu | \psi_J \rangle = \langle \Psi | \hat{\tau}_i^{\mu \dagger} \hat{\tau}_j^\nu | \Psi \rangle \quad (26)$$

Patches I and J can be any patches that respectively contain sites i and j . $\tau_{i \in I}^\mu = Q_I \hat{\tau}_i^\mu Q_I^\dagger$ denotes a truncated operator on patch I . Since patches I and J could be far apart, we insert a string of connections

$$V_{IJ}^{\text{string}} = V_{IK_1} V_{K_1 K_2} \cdots V_{K_l J} \quad (27)$$

to connect patches I and J , where $(I, K_1, K_2, \dots, K_l, J)$ is an arbitrary string of neighboring patches. To exactly encode the above correlation functions, Eq. (20) implies that it is sufficient for the images $\text{im}(Q_I^\dagger)$ to include the span of the actions of each operator on the wavefunction:

$$\text{im}(Q_I^\dagger) \supseteq \text{span} \{ | \Psi \rangle, \hat{\tau}_j^\mu | \Psi \rangle \text{ for each } \hat{\tau}_j^\mu \} \quad (28)$$

If there are M many operators $\hat{\tau}_i^\mu$, then the above image requires a QGN with bond dimension of at most $\chi_I = 1 + M$.

More generally, suppose we want to exactly encode all $2k$ -point correlation functions:

$$\begin{aligned} & \langle \Psi | \hat{\tau}_{i_1}^{\mu_1 \dagger} \cdots \hat{\tau}_{i_k}^{\mu_k \dagger} \hat{\tau}_{j_1}^{\nu_1} \cdots \hat{\tau}_{j_k}^{\nu_k} | \Psi \rangle \\ &= \langle \psi_{I_1} | \tau_{i_1 \in I_1}^{\mu_1 \dagger} V_{I_1, I_2}^{\text{string}} \cdots \tau_{i_k \in I_k}^{\mu_k \dagger} V_{I_k, J_1}^{\text{string}} \\ & \quad \tau_{j_1 \in J_1}^{\nu_1} V_{J_1, J_2}^{\text{string}} \cdots \tau_{j_k \in J_k}^{\nu_k} | \psi_{J_k} \rangle \end{aligned} \quad (29)$$

The left-hand-side is the expectation value of a product of $2k$ operators. The right-hand-side can be any corresponding expectation value within a QGN for any valid strings of connections. To exactly encode these correlation functions, Eq. (20) implies that it is sufficient

for the images to include the span of the actions of all products of up to k operators:

$$\text{im}(Q_I^\dagger) \supseteq \text{span} \left\{ \text{all } \prod_{r=1}^R \hat{\tau}_{j_r}^{\mu_r} | \Psi \rangle \text{ for } R = 0, 1, \dots, k \right\} \quad (30)$$

If there are M many operators $\hat{\tau}_i^\mu$, then there are

$$\chi = 1 + M + M^2 + \cdots + M^k \quad (31)$$

different operator products included in the span. Therefore, a QGN with bond dimension of at most χ is sufficient to encode all $2k$ -point correlation functions of M many operators.

Although the bond dimension increases exponentially with k , typically only few-body operators can be measured in experiments. Therefore, encoding k -point correlation functions with large k may not be necessary. On the other hand, for large systems, the number of operators M is large, and it is advantageous that χ only increases as a polynomial for large M and fixed k .

For a matrix product state (MPS), encoding all 2-point correlation functions generically requires an exponentially large bond dimension $\chi^{\text{MPS}} = 2^{M/6}$ for M many operators on a chain of qubits. For example, this exponential scaling is required when the wavefunction is a rainbow state. However, a matrix product operator (MPO) with bond dimension $O(M)$ is sufficient to encode all 2-point correlation functions. See Appendix C5 for details. Thus, QGN bond dimension scaling can be similar to that of an MPO.

See appendices C3 and C4 for analytical expressions of quantum gauge networks that exactly encode normal-ordered correlation functions of coherent boson wavefunctions and fermionic Slater determinant wavefunctions.

II. TIME EVOLUTION ALGORITHM

Since the quantum gauge network is closely related to the gauge picture [1] of quantum dynamics, we can straight-forwardly modify the gauge picture to obtain an approximate algorithm for simulating quantum dynamics using a QGN. To do this, we simply replace $|\Psi_I\rangle \rightarrow |\psi_I\rangle$, $\hat{U}_{IJ} \rightarrow V_{IJ}$, and $\hat{H}_{\langle I \rangle} \rightarrow H'_I$ (defined below) in the gauge picture equations of motion [Eq. (2)] to obtain:

$$\begin{aligned} \partial_t |\psi_I\rangle &= -i H'_I |\psi_I\rangle \\ \partial_t V_{IJ} &= -i H'_I V_{IJ} + i V_{IJ} H'_J \end{aligned} \quad (32)$$

If the Hamiltonian $\hat{H} = \sum_I \hat{H}_I$ [Eq. (1)] is a sum of local terms \hat{H}_I each supported on a spatial patch I , then we define

$$H'_I = \sum_{J \cap I \neq \emptyset} V_{IJ} H_J V_{JI} \quad (33)$$

$\sum_J^{J \cap I \neq \emptyset}$ sums over all patches J that have nontrivial overlap with the spatial patch I . H'_I is analogous to $\hat{H}_{\langle I \rangle}$ in the gauge picture [Eq. (3)]. Recall that H_I is a $\chi_I \times \chi_I$ matrix in the truncated Hilbert space, while \hat{H}_I is $N \times N$ and acts on the full N -dimensional Hilbert space. H_I can be obtained using the truncation mapping (11), which also holds when \hat{H}_I is time-dependent.

For time-independent Hamiltonians, the QGN approximation

$$E_{\text{QGN}}(t) = \sum_I \langle \psi_I(t) | H_I | \psi_I(t) \rangle \quad (34)$$

of the energy expectation value $\langle \Psi(t) | \hat{H} | \Psi(t) \rangle$ is conserved up to numerical integration errors for the time evolution in Eq. (32). See Appendix D for a proof.

For a QGN with bond dimension χ , the computation time of this algorithm is dominated by multiplication of $\chi \times \chi$ matrices. Therefore, the computation time for each time step scales as $O(n_V \chi^3)$, where n_V is the number of connections V_{IJ} used by the QGN. The memory cost scales as $O(n_V \chi^2)$ for storing the connections.³ For local Hamiltonians, n_V should be proportional to the number of lattice sites.

It is also possible to handle Hamiltonian terms that are not supported on a single spatial patch. Consider the Hamiltonian

$$\hat{H} = \sum_{J \cdots K} \sum_{\mu \cdots \nu} h_{J \cdots K}^{\mu \cdots \nu} \hat{\tau}_J^\mu \cdots \hat{\tau}_K^\nu \quad (35)$$

which consists of a sum $\sum_{J \cdots K}$ over spatial patches $J \cdots K$. $h_{J \cdots K}^{\mu \cdots \nu}$ are (generically time-dependent) real coefficients, and $\hat{\tau}_J^\mu$ denotes an operator indexed by μ with support on patch J . For example, we could take the patches to consist of a single qubit, and the $\hat{\tau}_J^\mu$ could be Pauli operators. For local Hamiltonians, $h_{J \cdots K}^{\mu \cdots \nu}$ will only be nonzero if $J \cdots K$ are close together. Equation (33) could be generalized to

$$H'_I = \sum_{J \cdots K}^{(J \cup \cdots K) \cap I \neq \emptyset} \sum_{\mu \cdots \nu} \frac{1}{2} h_{J \cdots K}^{\mu \cdots \nu} (V_{IJ} \tau_J^\mu V_{JI}) \cdots (V_{IK} \tau_K^\nu V_{KI}) + h.c. \quad (36)$$

³ Let $\tilde{\chi}_{IJ}$ be the number of non-zero singular values of V_{IJ} . If $\tilde{\chi}_{IJ} \ll \min(\chi_I, \chi_J)$, then it is more efficient to decompose $V_{IJ} = V_I^{(J)} V_J^{(I)\dagger}$ where $V_I^{(J)}$ is a $\chi_I \times \tilde{\chi}_{IJ}$ isometric matrix. If all $\chi_I = \chi$ and $\tilde{\chi}_{IJ} = \tilde{\chi}$ are equal, and if the H_I can be encoded as sparse matrices with $O(\chi)$ nonzero entries (which is typical), then the simulation and memory cost can respectively scale as $O(n_V \chi \tilde{\chi}^2)$ and $O(n_V \chi \tilde{\chi})$. This is asymptotically less costly when $\tilde{\chi} \ll \chi$. However for the simulations in this work, this decomposition is not useful since we chose connections for which $\tilde{\chi}/\chi$ only ranges from about 0.75 (in one spatial dimension) to 0.5 (in three spatial dimensions).

where $\sum_{J \cdots K}^{(J \cup \cdots K) \cap I \neq \emptyset}$ sums over spatial patches $J \cdots K$ such that the union $J \cup \cdots K$ has nontrivial overlap with patch I . “*h.c.*” denotes the Hermitian conjugate of the preceding terms and ensures that H'_I is Hermitian. When $J \cdots K$ involves more than two patches, we must decide on an ordering of the $J \cdots K$ for each I . Eq. (36) follows from a similar generalized expression for $\hat{H}_{\langle I \rangle}$ in the gauge picture [1] after projecting onto the Hermitian part (via the *h.c.*) and replacing $\hat{U}_{IJ} \rightarrow V_{IJ}$ and $\hat{\tau}_J^\mu \rightarrow \tau_J^\mu$. However, unlike for Eq. (33), the energy will not be conserved exactly for this choice of H'_I .

A. Fermion Quench

To benchmark this QGN algorithm, we simulate the dynamics of a quantum quench and compare to exact methods. First, we study the quench dynamics for a model of spinless fermions in one, two, and three spatial dimensions. In Appendix E, we also study the quench to a near-critical transverse field Ising model on a square lattice. In all cases, we find that increasing the bond dimension increases the simulation accuracy. This is as expected, since exact simulations of the gauge picture are reproduced once the bond dimension reaches the full Hilbert space dimension (or less when there are conserved quantities).

We initialize the system with a checkerboard pattern of spinless fermions, for which $\langle \hat{n}_i(0) \rangle = 1 - \langle \hat{n}_j(0) \rangle$ at time $t = 0$ for nearest-neighbor sites i and j ; as shown in Figs. 2a and 2d. We then time-evolve the system using the following Hamiltonian with nearest-neighbor hoppings and nearest-neighbor repulsive interactions:

$$\begin{aligned} \hat{H}^{\text{Fermi}} &= \sum_{\langle ij \rangle} \hat{H}_{\langle ij \rangle}^{\text{Fermi}} \\ \hat{H}_{I=\langle ij \rangle}^{\text{Fermi}} &= -\hat{c}_i^\dagger \hat{c}_j - \hat{c}_j^\dagger \hat{c}_i + V \hat{n}_i \hat{n}_j \end{aligned} \quad (37)$$

Each patch I is composed of a pair of nearest-neighbor sites, which are summed over by $\sum_{\langle ij \rangle}$ in the first line. \hat{c}_i is a fermion annihilation operator, and $\hat{n}_i = \hat{c}_i^\dagger \hat{c}_i$ is the fermion number operator.

We initialize the QGN using truncation maps, as described in Sec. IA. Choosing the truncation maps Q_I requires choosing a subspace of states to keep for each patch (i.e. a choice for the image of Q_I^\dagger , as in Sec. IB). We use the following method to select subspaces of states that we expect will acquire the highest weight after a short time evolution. (1) We begin with images of Q_I^\dagger that only contain the initial state. (2) For each patch I of nearest-neighbor sites, we add states to the image of Q_I^\dagger that can be obtained from the current image by swapping the two sites within the patch. (3) For each patch I , we add states that are included in patches J that overlap with patch I . (4) We repeat steps 2 and

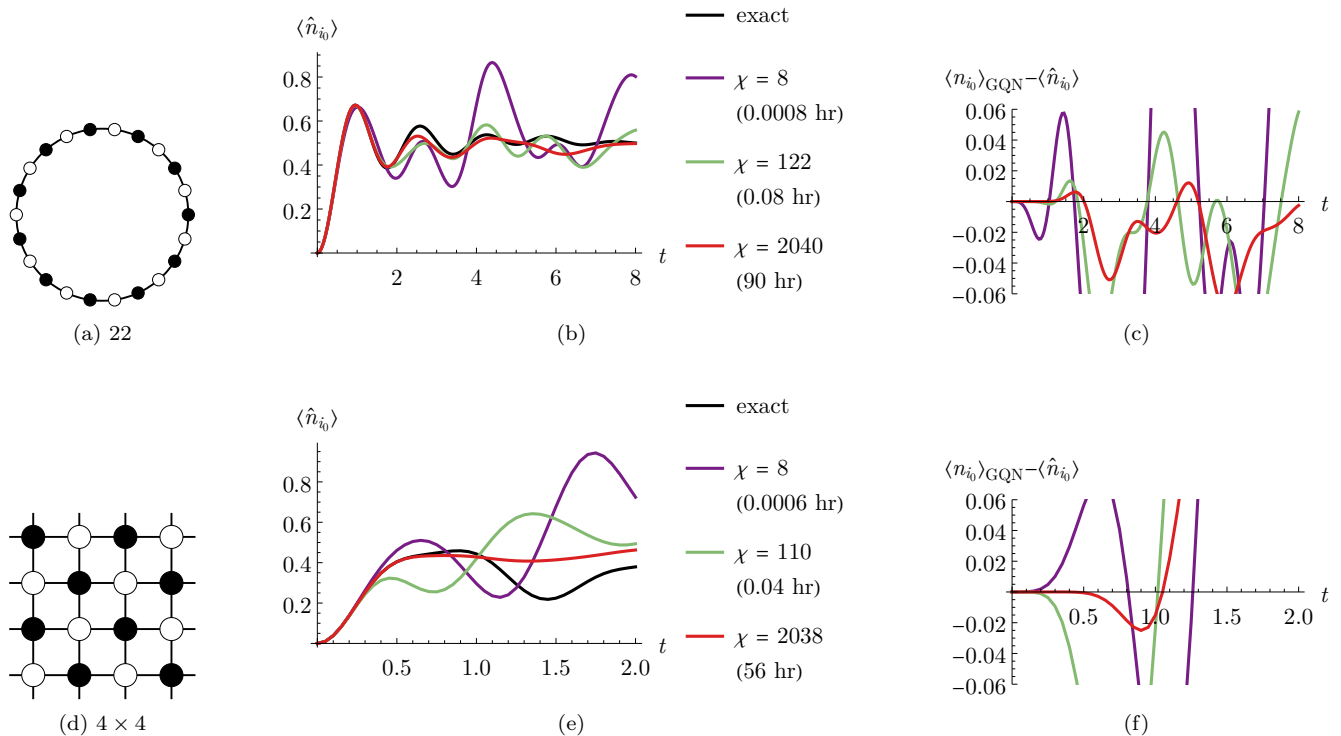


FIG. 2. Simulation data for the time dynamics of the fermionic Hamiltonian (37) with $V = 1$ following a quench from a checkerboard initial state in 1D and 2D periodic lattices. (a) An initial state of 11 spinless fermions (black disks) on a periodic chain of 22 sites (black and white disks). (b) Starting from this initial state, we show the fermion number expectation value $\langle \hat{n}_{i_0}(t) \rangle$ vs time t at a site i_0 with zero fermions at time $t = 0$. Simulation results are shown for the exact value (black line) and the quantum gauge network (QGN) with different bond dimensions χ (colored lines). The legend also shows the number of CPU core hours used for each simulation. (c) The error of the QGN approximation $\langle n_{i_0} \rangle_{\text{QGN}}$ [Eq. (38)] to the exact expression $\langle \hat{n}_{i_0} \rangle$. Panels (d-f) are similar, but for a periodic 4×4 square lattice. In both dimensions, we see that increasing the bond dimension increases the accuracy of the QGN simulations.

3 until we reach a bond dimension that is as large as desired.

With this initialization algorithm, we do not choose the bond dimension χ precisely (only roughly). This has the advantage that χ is chosen such that the QGN remains symmetric under lattice symmetries. Each image consists of a span of certain eigenstates of the number operators \hat{n}_i . Note that since the initial state has a definite fermion number, this procedure only adds states with the same fermion number, which is desirable since the Hamiltonian also conserves the fermion number. If we were to repeat steps 2 and 3 until no additional states could be added, then we would add all states with the initial fermion number and the QGN simulation would be exact.

We compare the quantum gauge network results to the exact values.⁴ Figure 2 shows one-dimensional (1D) and

two-dimensional (2D) simulation data with interaction strength $V = 1$. In both spatial dimensions, we find that the QGN can accurately simulate the dynamics for a short time, and the time over which the simulations are accurate increases with increasing bond dimension. The most time-consuming simulation consumed 90 CPU hours, which took less than half a day on an 8-core laptop.

We calculate the number expectation value $\langle \hat{n}_{i_0}(t) \rangle$ for sites i_0 that initially have zero fermions. In the QGN, these are estimated as follows:

$$\langle n_i \rangle_{\text{QGN}} = \sum_{I \ni i}^{\text{mean}} \langle \psi_I | n_{i \in I} | \psi_I \rangle \quad (38)$$

$\sum_{I \ni i}^{\text{mean}}$ averages over all patches I that contain the site i , and $n_{i \in I} = Q_I \hat{n}_i Q_I^\dagger$ is the truncated [Eq. (11)] number operator at site i for patch I . In this example, $\langle \psi_I | n_{i \in I} | \psi_I \rangle$ is equal for all patches I that contain site i due to spatial symmetries. However in other models with less symmetry, simulation errors can make these expectation values differ for different patches.

⁴ Exact expressions for small system sizes can be obtained by calculating the full wavefunction $|\Psi(t)\rangle = e^{-i\hat{H}t} |\Psi(0)\rangle$ using a sparse matrix representation for the Hamiltonian.

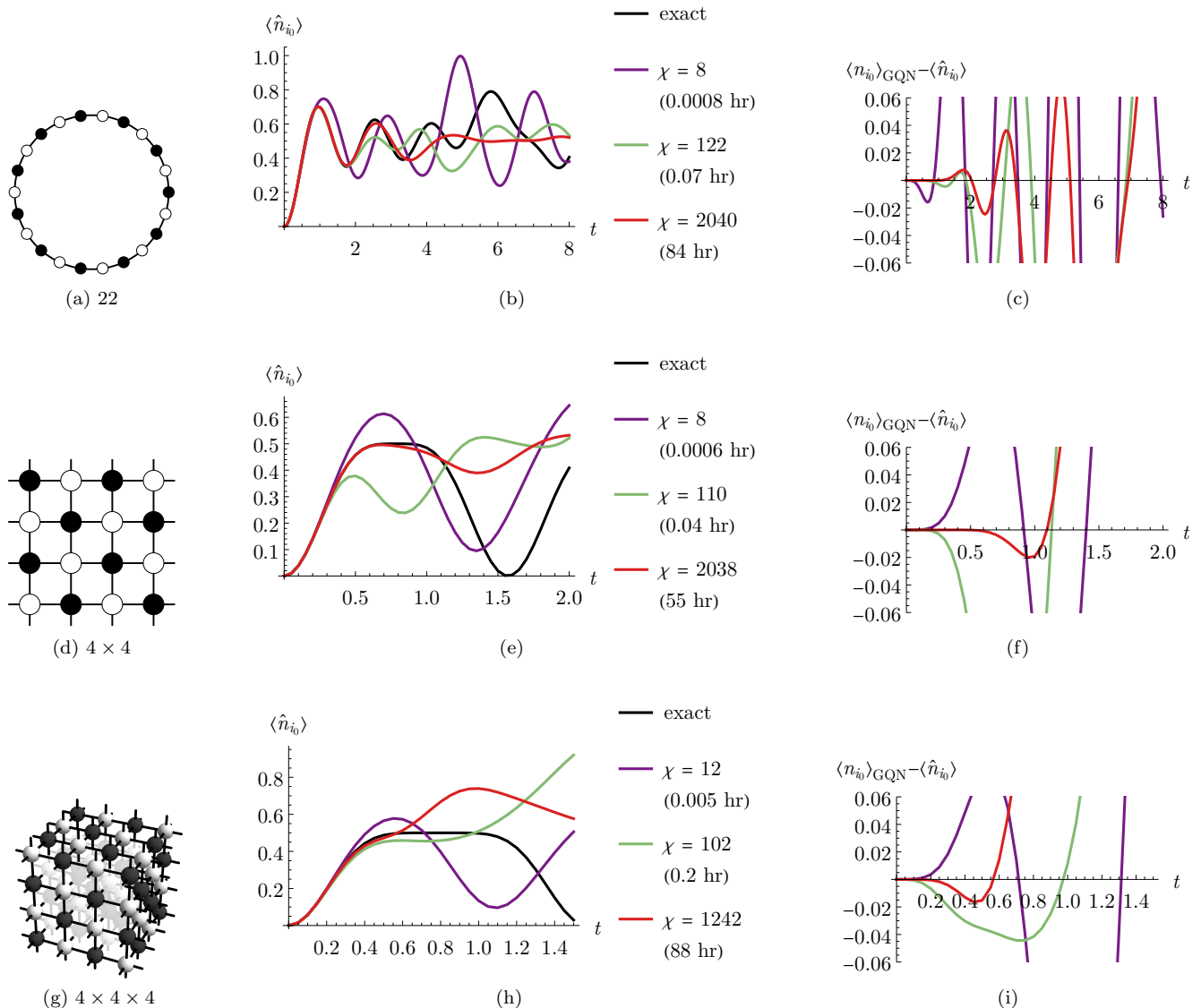


FIG. 3. Panels (a-f) are the same as Fig. 2, except we simulate non-interacting fermions with $V = 0$. By comparing to Fig. 2, we see that the QGN simulates $V = 0$ with roughly the same accuracy as $V = 1$. Panels (g-i) are similar, but for a periodic $4 \times 4 \times 4$ cubic lattice.

If we were to integrate the equations of motion exactly, then the energy expectation value [Eq. (34)] would be conserved exactly. Since exact integration is not practical, we use a modified RK4 Runge-Kutta method for numerical integration with time step $\delta_t = 0.05$. Due to this approximation, the energy per site changed by at most 10^{-3} for all data shown. See Appendix F for more details.

In order to compare to exact methods in three dimensions (3D) with many sites, we repeat the comparison in Fig. 3 with no interactions ($V = 0$). Free (i.e. non-interacting $V = 0$) fermion systems are efficient to simulate exactly [16] and are typically about as challenging for tensor network methods as interacting

fermionic systems. By comparing the 1D and 2D data in Figs. 2 and 3, we indeed see that $V = 1$ and $V = 0$ appear to be roughly equally challenging for the QGN. Therefore, we expect that the comparison we make for free fermions in 3D is representative of the interacting $V = 1$ model (for which we could not perform exact simulations). We find that accurate simulations can be maintained for a short period of time, which increases with the bond dimension and decreases with increasing spatial dimension.

For the free fermion simulations, the energy expectation value and total fermion number within the QGN appears to be conserved exactly (up to floating point precision). We have not yet investigated why this

conservation occurs in the free fermion system. When interactions ($V \neq 0$) are included, the QGN conserves the energy expectation value up to numerical integration errors, and the QGN fails to conserve the total charge expectation value.

III. OUTLOOK

Quantum gauge networks offer several advantages for simulating quantum dynamics, especially in comparison to many tensor network methods. (1) The computation time for simulating time dynamics is only χ^3 , where χ is the bond dimension. Notably, this computation time does not increase with the spatial dimension, which makes quantum gauge networks a promising tool in two or more dimensions. (2) Fermionic models are simple to handle. (Unlike MERA or PEPS, fermionic swap gate [17, 18] are not needed.) (3) The code is simple since the only tensors involved are vectors ψ_I and matrices V_{IJ} , and the code does not get more complicated in larger spatial dimensions. (4) The energy expectation value can be conserved (up to integration error). (5) Lattice symmetries can be maintained exactly. (6) Time discretization errors are small in practice since the dynamics can be integrated using very accurate Runge-Kutta methods. (Trotter-Suzuki expansions [19, 20] are not needed.)

There are numerous important future directions for the study of quantum gauge networks: (1) In comparison to other tensor networks, understanding quantum gauge networks is conceptually more demanding since the wavefunction is not directly encoded. The truncation mapping (10) is an example for which we can understand how the QGN relates to a wavefunction. But we do not know how to tell if a given QGN is consistent with any choice of wavefunction and truncation maps.⁵ We also do not know to what extent the truncation mapping can produce all quantum gauge networks that are useful approximations for quantum wavefunctions. (2) Can we optimize a QGN to find approximate ground states or excited eigenstates? This is relatively challenging for quantum gauge networks because a QGN can encode unphysical states, which means that some sort of (possibly approximate) constraint must be imposed on the QGN during energy minimization. (3) How well can a QGN encode topological states [24–28]?

There are also many opportunities to significantly improve our QGN time evolution algorithm: (4) For the TEBD algorithm [29], it is straightforward to increase or optimally truncate the bond dimension

during the simulation. In this work, we initialized the quantum gauge network using a simple basis of states in the number basis. We expect that this simple initialization is far from optimal, and that dynamically adding and removing more optimally chosen states throughout the time evolution could greatly improve simulation accuracy. (5) Can we obtain exact energy conservation when the Hamiltonian terms act on multiple spatial patches [as in Eq. (35)]? (6) Can we obtain charge conservation for charge-conserving Hamiltonians? (7) The TEBD algorithm allows one to upper-bound the simulation error in terms of the truncation error. Can we also estimate the error of a QGN time evolution without comparing to other algorithms? (8) Could we simulate infinite system sizes when the Hamiltonian is translation-invariant. (9) Finally, after improving QGN algorithms, benchmarking QGN methods against other methods [29–41] will be useful.

We find it intriguing that the consistency conditions ($V_{IJ}|\psi_J\rangle \approx |\psi_I\rangle$ and $V_{IJ}V_{JK} \approx V_{IK}$) in Eq. (7) are precisely the equations for a classical lattice gauge theory [42, 43] to be in its ground state when coupled to a Higgs field, where V_{IJ} plays the role of the gauge connection and $|\psi_I\rangle$ is the Higgs field. (See Appendix A for more details.) The primary difference is that in lattice gauge theory, the gauge connections are typically chosen to be unitary matrices. But V_{IJ} is not a unitary matrix; its singular values are only constrained to be between 0 and 1. With unitary gauge connections, no information is encoded locally in the classical ground state. (Information is only encoded in non-contractible Wilson loops.) It is remarkable that by simply relaxing the unitary constraint on the gauge connections (as in a QGN), ground states of classical lattice gauge theory coupled to a Higgs field are capable of locally encoding approximate quantum wavefunctions. Gauge theory plays a foundational role within the standard model of particle physics. As such, it may be interesting to study the emergent physics of quantum gauge networks, viewed not as a computational tool, but instead as a new kind of classical lattice gauge theory that exhibits aspects of emergent quantum mechanics [44–50].

We thank Lesik Motrunich, Gunhee Park, and Garnet Chan for helpful conversations. K.S. was partially supported by the Walter Burke Institute for Theoretical Physics at Caltech; and the U.S. Department of Energy, Office of Science, National Quantum Information Science Research Centers, Quantum Science Center.

⁵ This problem may be related to the QMA complete [21] quantum marginal problem [22, 23].

-
- [1] K. Slagle, (2022), [arXiv:arXiv:2210.09314](https://arxiv.org/abs/2210.09314).
 - [2] R. Orús, *Nature Reviews Physics* **1**, 538 (2019), [arXiv:1812.04011](https://arxiv.org/abs/1812.04011).
 - [3] R. Orús, *Annals of Physics* **349**, 117 (2014), [arXiv:1306.2164](https://arxiv.org/abs/1306.2164).

- [4] G. Kin-Lic Chan, A. Keselman, N. Nakatani, Z. Li, and S. R. White, [arXiv:1605.02611](#).
- [5] I. Cirac, D. Perez-Garcia, N. Schuch, and F. Verstraete, [arXiv:2011.12127](#).
- [6] S.-J. Ran, E. Tirrito, C. Peng, X. Chen, L. Tagliacozzo, G. Su, and M. Lewenstein, in *Tensor Network Contractions* (Springer, 2020) [arXiv:1708.09213](#).
- [7] J. C. Bridgeman and C. T. Chubb, *Journal of Physics A Mathematical General* **50**, 223001 (2017), [arXiv:1603.03039](#).
- [8] M. P. Zaletel and F. Pollmann, *Phys. Rev. Lett.* **124**, 037201 (2020), [arXiv:1902.05100](#).
- [9] K. Hyatt and E. M. Stoudenmire, [arXiv:1908.08833](#).
- [10] R. Haghshenas, M. J. O'Rourke, and G. K.-L. Chan, *Phys. Rev. B* **100**, 054404 (2019), [arXiv:1903.03843](#).
- [11] M. S. J. Tepaske and D. J. Luitz, *Physical Review Research* **3**, 023236 (2021), [arXiv:2005.13592](#).
- [12] G. Vidal, *Phys. Rev. Lett.* **101**, 110501 (2008), [arXiv:quant-ph/0610099](#).
- [13] G. Evenbly and G. Vidal, *Phys. Rev. Lett.* **112**, 240502 (2014), [arXiv:1210.1895](#).
- [14] G. Evenbly and G. Vidal, *Phys. Rev. B* **79**, 144108 (2009), [arXiv:0707.1454](#).
- [15] A. Acuaviva, V. Makam, H. Nieuwboer, D. Pérez-García, F. Sittner, M. Walter, and F. Witteveen, (2022), [arXiv:2209.14358](#).
- [16] The time dynamics of a free fermion Hamiltonian $\hat{H} = \sum_{ij} h_{ij} \hat{c}_i^\dagger \hat{c}_j$ can be simulated exactly by calculating the time-evolved filled single-fermion wavefunctions $|\phi_\alpha(t)\rangle = e^{-iht} |\phi_\alpha(0)\rangle$. The wavefunction $|\Psi\rangle = \prod_{\alpha}^{\text{filled}} (\sum_i \langle i|\phi_\alpha\rangle \hat{c}_i^\dagger) |0\rangle$ is never explicitly calculated. $\prod_{\alpha}^{\text{filled}}$ denotes the product over the filled single-fermion wavefunctions, and $|0\rangle$ is the empty state with no fermions. Then $\langle \hat{n}_i(t) \rangle = \sum_{\alpha}^{\text{filled}} |\langle i|\phi_\alpha(t)\rangle|^2$, where $|i\rangle$ is the single-fermion wavefunction for a fermion at site i .
- [17] R. Orús, *European Physical Journal B* **87**, 280 (2014), [arXiv:1407.6552](#).
- [18] P. Corboz and G. Vidal, *Phys. Rev. B* **80**, 165129 (2009), [arXiv:0907.3184](#).
- [19] A. M. Childs, Y. Su, M. C. Tran, N. Wiebe, and S. Zhu, *Phys. Rev. X* **11**, 011020 (2021), [arXiv:1912.08854](#).
- [20] B. Vanhecke, L. Vanderstraeten, and F. Verstraete, (2019), [arXiv:1912.10512](#).
- [21] Y.-K. Liu, in *Approximation, Randomization, and Combinatorial Optimization. Algorithms and Techniques*, edited by J. Díaz, K. Jansen, J. D. P. Rolim, and U. Zwick (Springer Berlin Heidelberg, Berlin, Heidelberg, 2006) pp. 438–449, [arXiv:quant-ph/0604166](#).
- [22] A. A. Klyachko, in *Journal of Physics Conference Series*, Journal of Physics Conference Series, Vol. 36 (2006) pp. 72–86, [arXiv:quant-ph/0511102](#).
- [23] J. Chen, Z. Ji, N. Yu, and B. Zeng, *Phys. Rev. A* **93**, 032105 (2016), [arXiv:1509.06591](#).
- [24] X.-G. Wen, *Reviews of Modern Physics* **89**, 041004 (2017), [arXiv:1610.03911](#).
- [25] Z.-C. Gu, M. Levin, B. Swingle, and X.-G. Wen, *Phys. Rev. B* **79**, 085118 (2009), [arXiv:0809.2821](#).
- [26] O. Buerschaper, M. Aguado, and G. Vidal, *Phys. Rev. B* **79**, 085119 (2009), [arXiv:0809.2393](#).
- [27] D. J. Williamson, N. Bultinck, and F. Verstraete, (2017), [arXiv:1711.07982](#).
- [28] T. Soejima, K. Siva, N. Bultinck, S. Chatterjee, F. Pollmann, and M. P. Zaletel, *Phys. Rev. B* **101**, 085117 (2020), [arXiv:1908.07545](#).
- [29] G. Vidal, *Phys. Rev. Lett.* **93**, 040502 (2004), [arXiv:quant-ph/0310089](#).
- [30] S. Paeckel, T. Köhler, A. Swoboda, S. R. Manmana, U. Schollwöck, and C. Hubig, *Annals of Physics* **411**, 167998 (2019), [arXiv:1901.05824](#).
- [31] S. R. White and A. E. Feiguin, *Phys. Rev. Lett.* **93**, 076401 (2004), [arXiv:cond-mat/0403310](#).
- [32] J. Haegeman, C. Lubich, I. Oseledets, B. Vandereycken, and F. Verstraete, *Phys. Rev. B* **94**, 165116 (2016), [arXiv:1408.5056](#).
- [33] E. Leviatan, F. Pollmann, J. H. Bardarson, D. A. Huse, and E. Altman, (2017), [arXiv:1702.08894](#).
- [34] C. B. Mendl, (2018), [arXiv:1812.11876](#).
- [35] P. Czarnik, J. Dziarmaga, and P. Corboz, *Phys. Rev. B* **99**, 035115 (2019), [arXiv:1811.05497](#).
- [36] D. Bauernfeind and M. Aichhorn, *SciPost Physics* **8**, 024 (2020), [arXiv:1908.03090](#).
- [37] T. Rakovszky, C. W. von Keyserlingk, and F. Pollmann, *Phys. Rev. B* **105**, 075131 (2022), [arXiv:2004.05177](#).
- [38] M. Yang and S. R. White, *Phys. Rev. B* **102**, 094315 (2020), [arXiv:2005.06104](#).
- [39] B. Kloss, D. Reichman, and Y. Bar Lev, *SciPost Physics* **9**, 070 (2020), [arXiv:2003.08944](#).
- [40] Á. M. Alhambra and J. I. Cirac, *PRX Quantum* **2**, 040331 (2021), [arXiv:2106.00710](#).
- [41] S.-H. Lin, M. Zaletel, and F. Pollmann, (2021), [arXiv:2112.08394](#).
- [42] G. Münster and M. Walzl, (2000), [arXiv:hep-lat/0012005](#).
- [43] J. B. Kogut, *Rev. Mod. Phys.* **51**, 659 (1979).
- [44] K. Slagle and J. Preskill, (2022), [arXiv:2207.09465](#).
- [45] S. Aaronson, in *Proceedings of the Thirty-Sixth Annual ACM Symposium on Theory of Computing*, STOC '04 (Association for Computing Machinery, New York, NY, USA, 2004) p. 118–127, [arXiv:quant-ph/0311039](#).
- [46] G. 't Hooft, (2020), [arXiv:2005.06374](#).
- [47] S. L. Adler, *Journal of Physics: Conference Series* **361**, 012002 (2012).
- [48] V. Vanchurin, *Foundations of Physics* **50**, 40 (2019), [arXiv:1901.07369](#).
- [49] E. Nelson, *Journal of Physics: Conference Series* **361**, 012011 (2012).
- [50] M. J. W. Hall, D.-A. Deckert, and H. M. Wiseman, *Physical Review X* **4**, 041013 (2014), [arXiv:1402.6144](#).
- [51] G. Vidal, *Phys. Rev. Lett.* **98**, 070201 (2007), [arXiv:cond-mat/0605597](#).
- [52] S. R. Garcia, M. Okubo Patterson, and W. T. Ross, (2019), [arXiv:1903.11648](#).
- [53] C. J. Hamer, *Journal of Physics A Mathematical General* **33**, 6683 (2000), [arXiv:cond-mat/0007063](#).

\hat{A}_i is an operator that only acts on site i .

It is also possible to obtain multiple simultaneous canonical forms, one for each $i = 1, 2, \dots, n$, while sharing the same isometries (L_i and R_i). These shared isometries obey

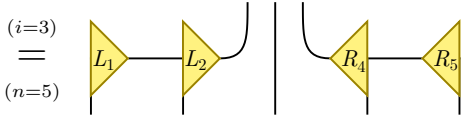
$$L_i^{(s_i)} C_{i+1}^{(s_{i+1})} = C_i^{(s_i)} R_{i+1}^{(s_{i+1})} \quad (\text{B5})$$

This simultaneous canonical form can be obtained by sweeping across the MPS multiple times using SVD decompositions or from the Vidal gauge [51]. The resulting bond dimensions of the $\chi_i^{\text{MPS}} \times d_i \times \chi_{i+1}^{\text{MPS}}$ tensors obey $\chi_i^{\text{MPS}} \leq d_i \chi_{i+1}^{\text{MPS}}$ and $\chi_i^{\text{MPS}} d_i \geq \chi_{i+1}^{\text{MPS}}$.

2. Quantum Gauge Network from MPS

To construct a quantum gauge network from an MPS, we choose Q_i^\dagger to map the truncated Hilbert space of the MPS orthogonality center C_i to the full Hilbert space:

$$Q_i^\dagger = \sum_{s_1 \dots s_n} \sum_{\alpha, \beta} \left(L_1^{(s_1)} \dots L_{i-1}^{(s_{i-1})} \right)_{1, \alpha} \left(R_{i+1}^{(s_{i+1})} \dots R_n^{(s_n)} \right)_{\beta, 1} |s_1 \dots s_n\rangle \langle \alpha s_i \beta| \quad (\text{B6})$$



Thus, Q_i^\dagger is just the canonical MPS centered at i , but with the orthogonality center C_i removed. Here, we choose the spatial patches to consist of just a single site, and we make no notational distinction between capital (I, J, K) and lower case (i, j, k) spatial indices letters.

Using Eq. (10) and the MPS canonical form identities [Eq. (B3)], we find that the local wavefunctions are equal to MPS orthogonality centers, while the connections are

equal to tensor products of two MPS isometries:

$$|\psi_i\rangle = \sum_{\alpha, s_i, \beta} (C_i^{(s_i)})_{\alpha, \beta} |\alpha s_i \beta\rangle$$

$$= \text{triangle } C_i$$

$$V_{i, i+1} = \sum_{\alpha, s_i, \alpha'} \sum_{\beta, s_{i+1}, \beta'} (L_i^{(s_i)})_{\alpha \alpha'} (R_{i+1}^{(s_{i+1})})_{\beta \beta'}^* |\alpha s_i \beta\rangle \langle \alpha' s_{i+1} \beta'| \quad (\text{B7})$$

We use the simultaneous canonical forms, which obey Eq. (B5) and guarantee that $V_{IJ} |\psi_J\rangle = |\psi_I\rangle$ [Eq. (12)] is satisfied.

The bond dimensions of the quantum gauge network are therefore $\chi_i = \chi_i^{\text{MPS}} d_i \chi_{i+1}^{\text{MPS}}$. The singular values of the $\chi_i \times \chi_{i+1}$ matrix $V_{i, i+1}$ consist of $(\chi_{i+1}^{\text{MPS}})^2$ ones, while the rest are zero. Thus, these $V_{i, i+1}$ are partial isometry matrices [52], which are matrices that obey $VV^\dagger V = V$ (or equivalently matrices whose singular values are either zero or one).

Appendix C: QGN Examples

In this appendix, we discuss several examples of quantum gauge networks.

1. Mixed State Example

As a simple example of a quantum gauge network, below we construct a QGN for the following mixed state of n qubits:

$$\hat{\rho}^{\text{mix}} = \frac{1}{2} |\uparrow_1 \uparrow_2 \dots \uparrow_n\rangle \langle \uparrow_1 \uparrow_2 \dots \uparrow_n| + \frac{1}{2} |\downarrow_1 \downarrow_2 \dots \downarrow_n\rangle \langle \downarrow_1 \downarrow_2 \dots \downarrow_n| \quad (\text{C1})$$

In order to apply the truncation mapping [Eq. (10)], we first find a purification of the density matrix:

$$|\Psi^{\text{mix}}\rangle = \frac{1}{\sqrt{2}} |\uparrow_0 \uparrow_1 \uparrow_2 \dots \uparrow_n\rangle + \frac{1}{\sqrt{2}} |\downarrow_0 \downarrow_1 \downarrow_2 \dots \downarrow_n\rangle \quad (\text{C2})$$

The wavefunction $|\Psi^{\text{mix}}\rangle$ hosts an additional auxiliary qubit with index $I = 0$. In this example, we take the spatial patches to consist of a single qubit. $|\Psi^{\text{mix}}\rangle$ is a purification of $\hat{\rho}^{\text{mix}}$ because tracing out the $I = 0$ qubit yields the density matrix: $\hat{\rho}^{\text{mix}} = \text{tr}_0 |\Psi^{\text{mix}}\rangle \langle \Psi^{\text{mix}}|$.

We follow Sec. **IB** to derive truncation maps Q_I by choosing the images $\text{im}(Q_I^\dagger)$ to be carefully chosen subspaces of states. To this end, we first note that any operator is a linear combination of Pauli strings, and the only Pauli strings with a nonzero expectation value for the state $\hat{\rho}^{\text{mix}}$ are products of $\hat{\sigma}_I^z \hat{\sigma}_J^z$ operators. Since the truncation mapping never increases the absolute value of expectation values [Eq. (13)], we therefore only need to ensure that expectation values of products of $\hat{\sigma}_I^z \hat{\sigma}_J^z$ operators are retained by the truncation. Equation (28) thus implies that we only need to include the action of a single $\hat{\sigma}_I^z$ in the image of Q_I^\dagger :

$$\begin{aligned} \text{im}(Q_I^\dagger) &= \text{span}\{ |\Psi^{\text{mix}}\rangle, \hat{\sigma}_I^z |\Psi^{\text{mix}}\rangle \} \\ &= \text{span}\{ |\uparrow_0 \uparrow_1 \cdots \uparrow_n\rangle, |\downarrow_0 \downarrow_1 \cdots \downarrow_n\rangle \} \end{aligned} \quad (\text{C3})$$

This image has dimension $\chi_I = 2$. A natural gauge choice for Q_I consistent with the above is:

$$\begin{aligned} Q_I &= |\uparrow\rangle \langle \uparrow_0 \uparrow_1 \uparrow_2 \cdots \uparrow_n| \\ &\quad + |\downarrow\rangle \langle \downarrow_0 \downarrow_1 \downarrow_2 \cdots \downarrow_n| \end{aligned} \quad (\text{C4})$$

Equation (10) then yields the following QGN:

$$\begin{aligned} |\psi_I\rangle &= \frac{1}{\sqrt{2}} |\uparrow\rangle + \frac{1}{\sqrt{2}} |\downarrow\rangle \\ V_{IJ} &= |\uparrow\rangle \langle \uparrow| + |\downarrow\rangle \langle \downarrow| \end{aligned} \quad (\text{C5})$$

with truncated operators [Eq. (11)]

$$\begin{aligned} \sigma_I^x &= \sigma_I^y = 0 \\ \sigma_I^z &= |\uparrow\rangle \langle \uparrow| - |\downarrow\rangle \langle \downarrow| \end{aligned} \quad (\text{C6})$$

This quantum gauge network exactly encodes all expectation values of the original reduced density matrix. For example,

$$\langle \psi_I | \sigma_I^\mu | \psi_I \rangle = \text{tr} \hat{\rho}^{\text{mix}} \hat{\sigma}_I^\mu = 0 \quad (\text{C7})$$

$$\langle \psi_I | \sigma_I^\mu V_{IJ} \sigma_J^\nu | \psi_J \rangle = \text{tr} \hat{\rho}^{\text{mix}} \hat{\sigma}_I^\mu \hat{\sigma}_J^\nu = \begin{cases} 1 & \mu = \nu = z \\ 0 & \text{otherwise} \end{cases}$$

a. Kronecker Product Operators

If we want to preserve the algebra of more of the truncated operators, then we should include their action in the images. For example, if we want to preserve the on-site algebra of the truncated Pauli operators, then we should instead choose:

$$\begin{aligned} \text{im}(Q_I^\dagger) &= \text{span}\{ |\Psi^{\text{mix}}\rangle, \hat{\sigma}_I^x |\Psi^{\text{mix}}\rangle, \hat{\sigma}_I^y |\Psi^{\text{mix}}\rangle, \hat{\sigma}_I^z |\Psi^{\text{mix}}\rangle \} \\ &= \text{span}\{ |\uparrow_0 \uparrow_1 \cdots \uparrow_n\rangle, \hat{\sigma}_I^x |\uparrow_0 \uparrow_1 \cdots \uparrow_n\rangle, \\ &\quad |\downarrow_0 \downarrow_1 \cdots \downarrow_n\rangle, \hat{\sigma}_I^x |\downarrow_0 \downarrow_1 \cdots \downarrow_n\rangle \} \end{aligned} \quad (\text{C8})$$

We can then pick the following truncation map:

$$\begin{aligned} Q_I &= |\uparrow_0 \uparrow_I\rangle \langle \uparrow_0 \uparrow_1 \uparrow_2 \cdots \uparrow_n| \\ &\quad + |\uparrow_0 \downarrow_I\rangle \langle \uparrow_0 \uparrow_1 \uparrow_2 \cdots \uparrow_n| \hat{\sigma}_I^x \\ &\quad + |\downarrow_0 \uparrow_I\rangle \langle \downarrow_0 \downarrow_1 \downarrow_2 \cdots \downarrow_n| \hat{\sigma}_I^x \\ &\quad + |\downarrow_0 \downarrow_I\rangle \langle \downarrow_0 \downarrow_1 \downarrow_2 \cdots \downarrow_n| \end{aligned} \quad (\text{C9})$$

The resulting QGN follows from Eq. (10):

$$\begin{aligned} |\psi_I\rangle &= \frac{1}{\sqrt{2}} |\uparrow_0 \uparrow_I\rangle + \frac{1}{\sqrt{2}} |\downarrow_0 \downarrow_I\rangle \\ V_{IJ} &= |\uparrow_0 \uparrow_I\rangle \langle \uparrow_0 \uparrow_J| + |\downarrow_0 \downarrow_I\rangle \langle \downarrow_0 \downarrow_J| \end{aligned} \quad (\text{C10})$$

Now the truncated Pauli operators are their natural Kronecker products:

$$\begin{aligned} \sigma_I^x &= \mathbb{1}_0 \otimes (|\uparrow_I\rangle \langle \downarrow_I| + |\downarrow_I\rangle \langle \uparrow_I|) \\ \sigma_I^y &= \mathbb{1}_0 \otimes (-i |\uparrow_I\rangle \langle \downarrow_I| + i |\downarrow_I\rangle \langle \uparrow_I|) \\ \sigma_I^z &= \mathbb{1}_0 \otimes (|\uparrow_I\rangle \langle \uparrow_I| + |\downarrow_I\rangle \langle \downarrow_I|) \end{aligned} \quad (\text{C11})$$

where $\mathbb{1}_0 = |\uparrow_0\rangle \langle \uparrow_0| + |\downarrow_0\rangle \langle \downarrow_0|$. These truncated operators obey their usual on-site algebra, e.g. $\sigma_I^x \sigma_I^y = i \sigma_I^z$.

2. Cat State Example

Encoding expectation values that act on many qubits in more than one spatial dimension is less straightforward. For example, consider the following cat state

$$\begin{aligned} |\Psi^{\text{cat}}\rangle &= \frac{1}{\sqrt{2}} |\uparrow_1 \uparrow_2 \cdots \uparrow_n\rangle \\ &\quad + \frac{1}{\sqrt{2}} |\downarrow_1 \downarrow_2 \cdots \downarrow_n\rangle \end{aligned} \quad (\text{C12})$$

The only Pauli string expectation value that can distinguish $|\Psi^{\text{cat}}\rangle$ from the mixed state $\hat{\rho}^{\text{mix}}$ in Eq. (C1) is the highly-nonlocal product of Pauli $\hat{\sigma}^x$ operators on every qubit:

$$\begin{aligned} \text{tr} \hat{\rho}^{\text{mix}} \prod_{I=1}^n \hat{\sigma}_I^x &= 0 \\ \left\langle \Psi^{\text{cat}} \left| \prod_{I=1}^n \hat{\sigma}_I^x \right| \Psi^{\text{cat}} \right\rangle &= 1 \end{aligned} \quad (\text{C13})$$

Any Pauli string that does not act on all qubits will have an equal expectation value for $\hat{\rho}^{\text{mix}}$ and $|\Psi^{\text{cat}}\rangle$.

Now suppose that $|\Psi^{\text{cat}}\rangle$ is a wavefunction for a square lattice of qubits. A quantum gauge network for $|\Psi^{\text{cat}}\rangle$ should reproduce the same nonlocal expectation value:

$$\langle \psi_1 | \sigma_1^x V_{12} \sigma_2^x \cdots V_{n-1,n} \sigma_n^x | \psi_n \rangle = 1 \quad (\text{C14})$$

where the sites $1, 2, \dots, n$ snake across the square lattice, as depicted in Fig. 4a. However, one may want other choices of paths [e.g. Fig. 4b or 4c] for this string operator to also lead to the same expectation value. This can be

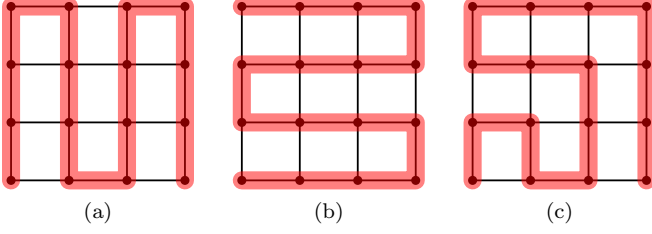


FIG. 4. Three different paths that cover all lattice sites.

achieved by adding these additional string operators to the procedure in Sec. IB at the cost of increasing the bond dimension. But if these additional string operators are not included in the QGN construction, then the expectation value of these excluded strings will be zero instead of one.

This example demonstrates the issue that a quantum gauge network can seem to encode different values for the same nonlocal expectation value depending on the path chosen. But if the QGN was obtained from the truncation mapping (10), then we at least know from Eq. (13) that the expectation value with the largest absolute value is the most accurate one.

3. Bosonic Coherent States

The normal ordered expectation values of bosonic coherent states can be encoded within a quantum gauge network in a rather trivial way. A bosonic coherent state is specified by complex numbers Θ_i and takes the following form:

$$|\Theta\rangle = \exp\left(\sum_i \Theta_i \hat{b}_i^\dagger\right) |0\rangle \quad (\text{C15})$$

\hat{b}_i is a boson annihilation operator, which satisfies the commutation relations $[\hat{b}_i, \hat{b}_j] = 0$ and $[\hat{b}_i, \hat{b}_j^\dagger] = \delta_{ij}$, and $|0\rangle$ is the vacuum state with no bosons: $\hat{b}_i |0\rangle = 0$.

The coherent state is an eigenstate of the annihilation operators: $\hat{b}_i |\Theta\rangle = \Theta_i |\Theta\rangle$. Therefore, if we only want the QGN to encode normal ordered expectation values, then Eq. (30) implies that the images of Q_I^\dagger only need to contain one state: $|\Theta\rangle$. We thus obtain a QGN with trivial bond dimensions $\chi_I = 1$ via the truncation map $Q_I = |\tilde{0}\rangle \langle \Theta|$. Here, $|\tilde{0}\rangle$ labels a state in a Hilbert space of dimension 1. With this truncation mapping, the local wavefunctions are $|\psi_I\rangle = |\tilde{0}\rangle$, and the connections are $V_{IJ} = |\tilde{0}\rangle \langle \tilde{0}| = \mathbb{1}$. The truncated [Eq. (11)] annihilation operator at a site i in patch I is simply

$$b_{i \in I} = Q_I \hat{b}_i Q_I^\dagger = \Theta_i \quad (\text{C16})$$

This QGN encodes all normal ordered expectation values

exactly, e.g.

$$\begin{aligned} \langle \Theta | \hat{b}_i^\dagger \hat{b}_j | \Theta \rangle &= \langle \psi_I | b_{i \in I}^\dagger V_{IJ} b_{j \in J} | \psi_J \rangle \\ &= \Theta_i^* \Theta_j \\ \langle \Theta | \hat{b}_i^\dagger \hat{b}_j^\dagger \hat{b}_k \hat{b}_l | \Theta \rangle &= \langle \psi_I | b_{i \in I}^\dagger V_{IJ} b_{j \in J}^\dagger V_{JK} b_{k \in K} V_{KL} b_{l \in L} | \psi_L \rangle \\ &= \Theta_i^* \Theta_j^* \Theta_k \Theta_l \end{aligned} \quad (\text{C17})$$

However, expectation values of operators that are not normal ordered are not encoded correctly by this QGN. For example, $\langle \psi_I | b_{i \in I} V_{IJ} b_{j \in J}^\dagger | \psi_J \rangle = \Theta_i^* \Theta_j$ while $\langle \Theta | \hat{b}_i \hat{b}_j^\dagger | \Theta \rangle = \delta_{ij} + \Theta_i^* \Theta_j$. These additional expectation values could be encoded exactly by adding additional states to the images $\text{im}(Q_I^\dagger)$, as outlined in Sec. IB 3.

4. Fermion Slater Determinants

We can analytically construct a quantum gauge network that exactly encodes all normal-ordered two-fermion correlation functions $\langle \hat{c}_i^\dagger \hat{c}_j \rangle$ for a fermionic Slater wavefunction. If there are n_f filled states, we can construct a QGN with bond dimension $\chi_I = 1 + n_f$. This is more efficient than the $1 + M$ upper bound in Eq. (31), where $M = n$ is the number of operators whose correlation functions we wish to encode; here we consider all fermion annihilation operators \hat{c}_i with $i = 1, \dots, n$.

A Slater determinant wavefunction can be expressed as

$$|\Phi\rangle = \prod_{\alpha=1}^{n_f} \sum_{i=1}^n \Phi_{\alpha i} \hat{c}_i^\dagger |0\rangle \quad (\text{C18})$$

using second-quantized Fock states. $i = 1, \dots, n$ indexes the n different single-particle states. \hat{c}_i is a fermion annihilation operator, which satisfies the anticommutation relations $\{\hat{c}_i, \hat{c}_j\} = 0$ and $\{\hat{c}_i, \hat{c}_j^\dagger\} = \delta_{ij}$. We fill K many fermion orbitals, which are indexed by α and encoded by the matrix elements $\Phi_{\alpha i}$. The orbitals are assumed to be orthonormalized: $\Phi \cdot \Phi^\dagger = \mathbb{1}$. The inner product of two Slater determinant wavefunctions is $\langle \Phi | \Phi' \rangle = \det(\Phi' \cdot \Phi^\dagger)$.

The action of an annihilation operator on a Slater determinant wavefunction is

$$\hat{c}_i |\Phi\rangle = \sum_{\alpha=1}^K (-1)^{\alpha-1} \Phi_{\alpha i} |\Phi_\alpha^-\rangle \quad (\text{C19})$$

We define

$$|\Phi_\alpha^-\rangle = \prod_{\alpha' \neq \alpha} \sum_i \Phi_{\alpha' i} \hat{c}_i^\dagger |0\rangle \quad (\text{C20})$$

to be the Slater determinant wavefunction where we do not fill orbital α , but the other $n_f - 1$ orbitals are still filled.

Equation (28) implies that the images of Q_I^\dagger only need to contain the states $|\Phi\rangle$ and $|\Phi_\alpha^-\rangle$. Let $|\phi\rangle$ and $|\phi_\alpha^-\rangle$ label

a basis of $1 + n_f$ states for the local QGN Hilbert spaces. Then we can choose truncation maps

$$Q_I = |\phi\rangle \langle \Phi| + \sum_{\alpha=1}^{n_f} |\phi_\alpha^-\rangle \langle \Phi_\alpha^-| \quad (\text{C21})$$

With this choice, the local wavefunctions are $|\psi_I\rangle = Q_I |\Phi\rangle = |\phi\rangle$, and the connections are $V_{IJ} = Q_I Q_J^\dagger = \mathbb{1}$. The truncated fermion operators follow from Eq. (C19):

$$c_{i \in I} = Q_I \hat{c}_i Q_I^\dagger = \sum_{\alpha=1}^K (-1)^{\alpha-1} \Phi_{\alpha i} |\phi_\alpha^-\rangle \langle \phi| \quad (\text{C22})$$

This QGN exactly encodes all normal-ordered two-fermion correlation functions:

$$\begin{aligned} \langle \Phi | \hat{c}_i^\dagger \hat{c}_j | \Phi \rangle &= \langle \psi_I | c_{i \in I}^\dagger V_{IK_1} V_{K_1 K_2} \cdots V_{K_l J} c_{j \in J} | \psi_J \rangle \\ &= (\Phi^\dagger \cdot \Phi)_{ij} \end{aligned} \quad (\text{C23})$$

where $V_{IK_1} V_{K_1 K_2} \cdots V_{K_l J}$ is any string of connections that connect patches I and J .

Above, we only worked out analytical expressions for two-fermion correlation functions. However, analytical expressions for many-fermion correlation functions should also be possible. The above QGN is rather trivial in the sense that the connections V_{IJ} are all identity matrices. This is because we did not take advantage of spatial locality. If many of the fermion orbitals are spatially local, we expect that an approximate QGN encoding can be achieved with significantly smaller bond dimensions and non-identity V_{IJ} .

5. Rainbow State

In Sec. IB3, we showed that all $2k$ -point correlation functions of M many operators can be encoded exactly by a QGN with bond dimension $O(M^k)$. This is significantly more efficient than a matrix product state (MPS), which can require bond dimension $\chi^{\text{MPS}} = 2^{n/2}$ to encode all two-point correlation functions of certain states with n qubits, e.g. the rainbow state. In the n -qubit rainbow state, pairs of qubits i and $n+1-i$ are maximally entangled in a Bell state. The two-point correlation functions of the rainbow state are $\langle \hat{\sigma}_i^\mu \hat{\sigma}_j^\nu \rangle = \delta_{\mu\nu} \delta_{n+1-i,j}$. $\delta_{\mu\nu}$ denotes the Kronecker delta function. The rainbow state is the unique state with these correlation functions. Therefore, in order for an MPS to encode these 2-point correlation functions, the MPS must encode the rainbow state. Encoding the rainbow state requires MPS bond dimension $\chi^{\text{MPS}} = 2^{n/2} = 2^{M/6}$, where $M = 3n$ is the number of Pauli operators $\hat{\sigma}_i^\mu$ for n qubits.

However, a matrix product operator (MPO) with bond dimension $\chi^{\text{MPO}} = 1 + M/2$ is sufficient to encode the 2-point correlation functions of the rainbow state by encoding the (unphysical) density matrix

$\hat{\rho} = \hat{\mathbb{1}} + \sum_{i=1}^{n/2} \sum_{\mu=x,y,z} \hat{\sigma}_i^\mu \hat{\sigma}_{n+1-i}^\mu$. This density matrix is unphysical because it has negative eigenvalues. (A QGN bond dimension of $\chi = 1 + M/2$ would also be sufficient for this example if we restrict the allowed operator strings to never change direction.)

Appendix D: Energy Conservation

Below, we prove that the QGN equations of motion [Eq. (32)] preserve the energy expectation value [Eq. (34)] exactly when the local Hamiltonian terms \hat{H}_I are time-independent and each supported on a single spatial patch [as in Eqs. (1) and (33)].

$$\begin{aligned} &\partial_t \sum_I \langle \psi_I | H_I | \psi_I \rangle \\ &= \sum_I i \langle \psi_I | [H'_I, H_I] | \psi_I \rangle \\ &= \sum_{I \cap J \neq \emptyset} i \langle \psi_I | [V_{IJ} H_J V_{JI}, H_I] | \psi_I \rangle \\ &= \sum_{I \cap J \neq \emptyset} \frac{i}{2} \langle \psi_I | [V_{IJ} H_J V_{JI}, H_I] | \psi_I \rangle \\ &\quad + \frac{i}{2} \langle \psi_J | [V_{JI} H_I V_{IJ}, H_J] | \psi_J \rangle \\ &= \sum_{I \cap J \neq \emptyset} \frac{i}{2} \langle \psi_I | [V_{IJ} H_J V_{JI}, H_I] + [H_I, V_{IJ} H_J V_{JI}] | \psi_I \rangle \\ &= 0 \end{aligned} \quad (\text{D1})$$

The first three equalities respectively follow from Eq. (32) for $\partial_t |\psi_I\rangle$; Eq. (33) for H'_I ; and symmetrizing the sum over $I \leftrightarrow J$. $\sum_{I \cap J \neq \emptyset}$ denotes the sum over all patches I and J that have nonzero overlap. The final equality follows from the antisymmetry of the commutator. The second to last equality follows from:

$$\begin{aligned} &\langle \psi_J | [V_{JI} H_I V_{IJ}, H_J] | \psi_J \rangle \\ &= \langle \psi_J | V_{JI} H_I V_{IJ} H_J - H_J V_{JI} H_I V_{IJ} | \psi_J \rangle \\ &= \langle \psi_I | H_I V_{IJ} H_J V_{JI} - V_{IJ} H_J V_{JI} H_I | \psi_I \rangle \\ &= \langle \psi_I | [H_I, V_{IJ} H_J V_{JI}] | \psi_I \rangle \end{aligned} \quad (\text{D2})$$

which follows from $V_{IJ} |\psi_J\rangle = |\psi_I\rangle$ [Eq. (12)].

Appendix E: Ising Model Quench

In this appendix, we benchmark the quantum gauge network by studying the dynamics following a quench to a near-critical Ising model. We start from the initial state $|\Psi(0)\rangle = \otimes_i |-\rangle_i$ where all $\langle \sigma_i^x \rangle = 1$, and then we time evolve with a near-critical transverse field Ising

Hamiltonian

$$\hat{H}^{\text{Ising}} = - \sum_{\langle ij \rangle} \hat{\sigma}_i^z \hat{\sigma}_j^z - h \sum_i \hat{\sigma}_i^x \quad (\text{E1})$$

with $h = 3$ on a two-dimensional 4×4 square lattice with periodic boundary conditions. (The critical point is at $h_c \approx 3.045$ [53].) This system size is chosen so that we can compare to exact methods that calculate the full wavefunction $|\Psi(t)\rangle = e^{-i\hat{H}^{\text{Ising}}t} |\Psi(0)\rangle$.

In order to make use of Eqs. (1) and (33), we define the Hamiltonian \hat{H}_I on each spatial patch to be

$$\hat{H}_{I=\langle ij \rangle}^{\text{Ising}} = -\hat{\sigma}_i^z \hat{\sigma}_j^z - \frac{1}{4}h(\hat{\sigma}_i^x + \hat{\sigma}_j^x) \quad (\text{E2})$$

We take each spatial patch I to be a pair of nearest-neighbor sites $\langle ij \rangle$. Note that in the sum $\hat{H} = \sum_I \hat{H}_I$ from Eq. (1), each site is summed over four times on a square lattice; thus we require the above $\frac{1}{4}$ factor in front of h .

We initialize the QGN using truncation maps (as described in Sec. IA), which are chosen using a method similar to the one described in Sec. II A. However in this spin model, we do not have a conserved charge. Therefore, we modify step 2 of the method in Sec. IA [paragraph below Eq. (37)] to the following: (2) For each patch I , we add states to the image of Q_I^\dagger that can be obtained from the current image of Q_I^\dagger by acting with Pauli operators within the patch I .

The truncation at each patch I only retains states consisting of a span of eigenstates of the $\hat{\sigma}_i^x$ operators. With a natural gauge choice for the truncation maps, the truncated Pauli operators take the form of a Kronecker product:

$$\sigma_{i \in I}^\mu = Q_I \hat{\sigma}_i^\mu Q_I^\dagger = \mathbb{1} \otimes \sigma^\mu \quad (\text{E3})$$

$\sigma_{i \in I}^\mu$ is the truncated [Eq. (11)] Pauli operator at site i for patch I , and σ^μ is a 2×2 Pauli matrix.

In Fig. 5, we show QGN simulation data for Pauli expectation values $\langle \hat{\sigma}_i^\mu(t) \rangle$ and compare to the exact values. We see that the simulation errors decrease as we increase the bond dimension.

In the QGN, the expectation values are estimated as

$$\langle \hat{\sigma}_i^\mu \rangle_{\text{QGN}} = \sum_{I \ni i}^{\text{mean}} \langle \psi_I | \sigma_{i \in I}^\mu | \psi_I \rangle \quad (\text{E4})$$

where $\sum_{I \ni i}^{\text{mean}}$ averages over all patches I that contain the site i . In this example, $\langle \psi_I | \sigma_{i \in I}^\mu | \psi_I \rangle$ is equal for all patches I that contain site i due to spatial symmetries. However in other models with less symmetry, simulation errors can make these expectation values differ for different patches.

If we were to integrate the equations of motion exactly, then the energy expectation value [Eq. (34)] would be conserved exactly. Since exact integration is not

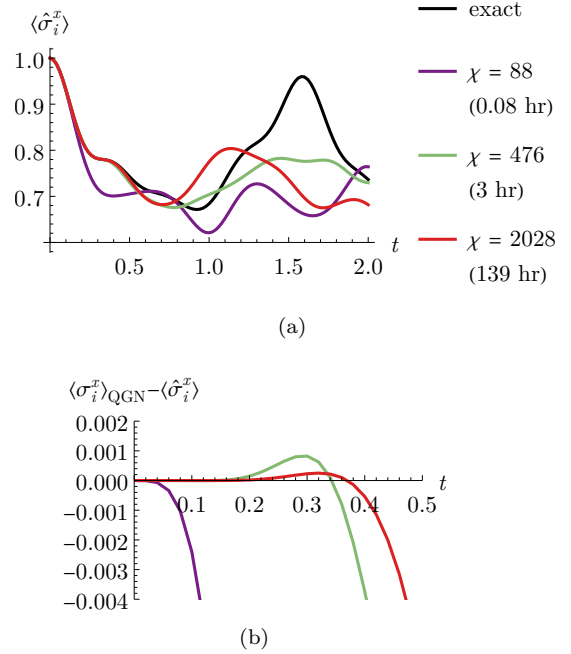


FIG. 5. Simulation data for the time dynamics of the near-critical transverse field Ising Hamiltonian (E1) on a periodic 4×4 square lattice following a quench from the state $|\Psi(0)\rangle = \otimes_i |\rightarrow_i\rangle$. (a) The quantum gauge network (QGN) approximation for $\langle \hat{\sigma}_i^x \rangle$ vs time t for different bond dimensions χ (colored lines) vs the exact value (black line). The legend also shows the number of CPU core hours used for each simulation. Due to symmetry, the $\langle \sigma_i^y \rangle$ and $\langle \sigma_i^z \rangle$ expectation values (not shown) are exactly zero for all time for both the QGN and the exact value. (b) The error $\langle \sigma_i^x \rangle_{\text{QGN}} - \langle \hat{\sigma}_i^x \rangle_{\text{exact}}$ of the QGN approximation to $\langle \hat{\sigma}_i^x \rangle$. The error stays small for longer times as we increase the bond dimension χ .

practical, we use a modified RK4 Runge-Kutta method for integration with time step $\delta_t = 0.02$. Due to this approximation, the energy per site changed by 5×10^{-4} and 1×10^{-4} for the $\chi = 88$ and 2028 simulations, respectively. See Appendix F for more details.

Appendix F: Modified Runge-Kutta

We use a modified RK4 Runge-Kutta method to integrate the differential equations. RK4 is a fourth-order Runge-Kutta method that results in an $O(\delta_t^4)$ error at time $t \sim 1$, where δ_t is the time step size. However, the straight-forward application of Runge-Kutta will not preserve $V_{IJ} |\psi_J\rangle = |\psi_I\rangle$ [Eq. (12)] exactly; it will only be preserved up to $O(\delta_t^4)$ error. In this work, we chose to modify the Runge-Kutta method slightly such that $V_{IJ} |\psi_J\rangle = |\psi_I\rangle$ is preserved exactly (i.e. up to floating point precision). We end up making an additional approximation that increases the simulation error to $O(\delta_t^3)$ (which we were satisfied with). It would be useful to improve the approximation such that $O(\delta_t^4)$

and smaller errors can be achieved while maintaining $V_{IJ}|\psi_J\rangle = |\psi_I\rangle$.

Instead of integrating $\partial_t |\psi_I\rangle$ and $\partial_t V_{IJ}$ directly at each time step, we use a modified Runge-Kutta method to obtain estimates for the unitary evolution

$$U_I^{\text{RK}}(t + \delta_t, t) = e^{-i\delta_t H_I^{\text{RK}}(t)} \quad (\text{F1})$$

We then update the QGN from time t to $t + \delta_t$ as follows:

$$\begin{aligned} |\psi_I(t + \delta_t)\rangle &= U_I^{\text{RK}}(t + \delta_t, t) |\psi_I(t)\rangle \\ V_{IJ}(t + \delta_t) &= U_I^{\text{RK}}(t + \delta_t, t) V_{IJ}(t) U_J^{\text{RK}}(t + \delta_t, t)^\dagger \end{aligned} \quad (\text{F2})$$

We obtain

$$H_I^{\text{RK}}(t) = \sum_{k=1}^s b_k \tilde{H}_I^{(k)}(t) \quad (\text{F3})$$

using the Runge-Kutta coefficients b_k , where s is the number of Runge-Kutta stages. $s = 4$ for RK4.

In order to calculate $\tilde{H}_I^{(k)}(t)$, we first recursively define $H_I^{(k)}(t + c_k \delta_t)$ (without the tilde), which we set equal to H_I' [Eq. (33)] at time $t + c_k \delta_t$ evaluated using the QGN that is updated from time t to $t + c_k \delta_t$ by the unitary

$$\tilde{U}_I^{(k)}(t + c_k \delta_t, t) = e^{-i \sum_{l=1}^{k-1} a_{kl} \delta_t \tilde{H}_I^{(l)}(t)} \quad (\text{F4})$$

via Eq. (F2) (with $\tilde{U}_I^{(k)}$ and $t + c_k \delta_t$ in place of U_I^{RK} and $t + \delta_t$). a_{kl} and c_k are additional Runge-Kutta coefficients. For $k = 1$, $c_1 = 0$ and $\tilde{H}_I^{(1)} = H_I^{(1)} = H_I'$ at time t . We find that choosing $\tilde{H}_I^{(l)}(t) = H_I^{(l)}(t + c_k \delta_t)$ results in $O(\delta_t^2)$ simulation errors after time $t \sim 1$ using the RK4 coefficients. We instead use

$$\begin{aligned} \tilde{H}_I^{(l)}(t) &= \frac{1}{2} \tilde{U}_I^{(l)}(t + c_l \delta_t, t)^\dagger H_I^{(l)}(t + c_k \delta_t) \tilde{U}_I^{(l)}(t + c_l \delta_t, t) \\ &\quad + \frac{1}{2} H_I^{(l)}(t + c_k \delta_t) \end{aligned} \quad (\text{F5})$$

for which we observe an $O(\delta_t^3)$ simulation error after time $t \sim 1$. For RK4, the tableau of coefficients is

$$\begin{array}{c|ccc} c_1 & & & 0 \\ c_2 & a_{21} & & 1/2 \\ c_3 & a_{31} & a_{32} & 1/2 \\ c_4 & a_{41} & a_{42} & a_{43} \\ \hline & b_1 & b_2 & b_3 & b_4 \end{array} = \begin{array}{c|ccc} & & & 0 \\ & & & 1/2 \\ & & & 1/2 \\ & & & 1 \\ \hline & & & 0 & 0 & 1 \\ \hline & & & 1/6 & 1/3 & 1/3 & 1/6 \end{array} \quad (\text{F6})$$